eNeuro Accepted Manuscript

eNeuro

Research Article: New Research | Neuronal Excitability

Loss of KCNQ2 or KCNQ3 leads to multifocal time-varying activity in the neonatal forebrain *ex vivo*

https://doi.org/10.1523/ENEURO.0024-21.2021

Cite as: eNeuro 2021; 10.1523/ENEURO.0024-21.2021

Received: 19 January 2021
Revised: 5 April 2021
Accepted: 8 April 2021

This Early Release article has been peer-reviewed and accepted, but has not been through the composition and copyediting processes. The final version may differ slightly in style or formatting and will contain links to any extended data.

Alerts: Sign up at www.eneuro.org/alerts to receive customized email alerts when the fully formatted version of this article is published.

Copyright © 2021 Hou et al.
This is an open-access article distributed under the terms of the Creative Commons Attribution 4.0 International license, which permits unrestricted use, distribution and reproduction in any medium provided that the original work is properly attributed.

eNeuro Accepted Manuscript

Loss of KCNQ2 or KCNQ3 leads to multifocal time-varying activity in the neonatal forebrain *ex vivo*

Abbreviated title: KCNQ2, KCNQ3 ablation leads to multifocal activity

Bowen Hou[1], Nissi Varghese[1], Heun Soh[1], Sabato Santaniello[2*], and Anastasios V. Tzingounis[1,2*]
[1]Dept. of Physiology and Neurobiology, University of Connecticut, Storrs, CT 06269, USA. [2]Dept. of Biomedical Engineering, University of Connecticut, Storrs, CT 06269, USA.

Author contributions: BH, SS, and AVT Designed research; BH, NV and HS Performed research; BH and SS Analyzed data; BH, SS, AVT Wrote the paper

***Co-Correspondence:**
Anastasios Tzingounis, PhD
Department of Physiology and Neurobiology University of Connecticut
Storrs, CT 06269, USA
Email: anastasios.tzingounis@uconn.edu

Sabato Santaniello, PhD
Department of Biomedical Engineering
University of Connecticut
Storrs, CT 06269, USA
Email: sabato.santaniello@uconn.edu

Number of figures: 13
Number of Tables: 1
Number of Multimedia: 4
Number of words in Abstract: 192
Number of words for Significance Statement: 68
Number of words for Introduction: 651
Number of words for Discussion: 1233

Acknowledgments: We thank all members of the Tzingounis lab for discussions.

Conflict of Interest: The authors declare no financial or conflicts of interests.

Funding sources: This work was supported by National Institutes of Health Grants R01 NS101596, HL137094, NS108874 (to AVT), and NSF CAREER Award 1845348 (to S.S).

eNeuro Accepted Manuscript

ABSTRACT

Early neonatal epileptic encephalopathy represents a group of epilepsies often characterized by refractory seizures, regression in cognitive development, and typically poor prognosis. Dysfunction of KCNQ2 and KCNQ3 channels has emerged as a major cause of neonatal epilepsy. However, our understanding of the cellular mechanisms that may both explain the origins of epilepsy and inform treatment strategies for KCNQ2 and KCNQ3 dysfunction is still lacking. Here, using mesoscale calcium imaging and pharmacology, we demonstrate that in mouse neonatal brain slices, conditional loss of *Kcnq2* from forebrain excitatory neurons (*Pyr:Kcnq2* mice) or constitutive deletion of *Kcnq3* leads to sprawling hyperactivity across the neocortex. Surprisingly, the generation of time-varying hypersynchrony in slices from *Pyr:Kcnq2* mice does not require fast synaptic transmission. This is in contrast to control littermates and constitutive *Kcnq3* knockout mice where activity is primarily driven by fast synaptic transmission in the neocortex. Unlike in the neocortex, hypersynchronous activity in the hippocampal formation from *Kcnq2* conditional and *Kcnq3* constitutive knockout mice persists in the presence of synaptic transmission blockers. Thus, we propose that loss of KCNQ2 or KCNQ3 function differentially leads to network hyperactivity across the forebrain in a region- and macro-circuit-specific manner.

eNeuro Accepted Manuscript

SIGNIFICANCE STATEMENT

Neocortical hypersynchrony is a hallmark of neonatal epilepsy but its cellular mechanisms are unclear. This study shows that hypersynchrony in the neocortex can stem from the loss of KCNQ2 function in excitatory neurons even in the absence of fast synaptic transmission, unlike the hypersynchrony in response to KCNQ3 loss in the neocortex. This points to unique network dysfunctions involving potassium KCNQ2 channels as a mechanism for neonatal epilepsy.

eNeuro Accepted Manuscript

INTRODUCTION

Ion channelopathies have been associated with multiple neurodevelopmental disorders over the last decades (Satterstrom et al., 2020; Wang et al., 2020). The KCNQ family, otherwise known as the Kv7 family, is a potassium channel family that has been propelled at the forefront of neurodevelopmental disorders (Geisheker et al., 2017; Cornet et al., 2018). Several of its members (KCNQ2-KCNQ5) are expressed in the brain, across multiple brain regions and cell types (Greene and Hoshi, 2017). KCNQ2 channels were the second members of this family to be identified, with a rich history relating to neurodevelopmental disorders. *KCNQ2* was first discovered over 20 years ago as a gene likely to cause benign familial neonatal seizures, a form of a self-limiting pediatric epilepsy disorder (Jentsch, 2000). However, since 2012, multiple studies have shown that *KCNQ2* variants may lead to a large spectrum of symptoms and disorders, including Ohtahara syndrome and autism spectrum disorders (Cornet et al., 2018). These studies have demonstrated that *KCNQ2* pathogenicity leads to Developmental and Epileptic Encephalopathies (DEE).

Over the years, our knowledge regarding KCNQ2 channel function in the brain has grown exponentially. This understanding has primarily arisen from the use of *Kcnq2* transgenic mice and pharmacological agents that generally target KCNQ2-containing channels. KCNQ2 channels partner with KCNQ3 channels to form heteromeric channels containing two KCNQ2 and two KCNQ3 channels, classically referred to as the M-channels, as they mediate the M-current, a ubiquitous potassium conductance discovered in the 1980s (Jentsch, 2000). KCNQ2/3 channels are strategically located at

eNeuro Accepted Manuscript

sites of action potential initiation and regeneration, allowing them to control neuronal excitability by regulating the resting membrane potential of the axon initial segment and axons by preventing excessive firing (Cooper, 2011). Indeed, *Kcnq2* deletion or expression of KCNQ2 pathogenic variants in neurons leads to elevated excitability, typically manifested as a higher number of action potentials and reduced spike frequency adaptation. Such changes in excitability occur in multiple brain regions, including the hippocampus and neocortex, and across multiple cell types (Peters et al., 2005; Singh et al., 2008; Soh et al., 2014; Soh et al., 2018; Verneuil et al., 2020).

To date, most studies on KCNQ2 and KCNQ3 channels using transgenic mice have focused on excitatory neurons in juvenile and adult mice. However, KCNQ2 channels are expressed early in development, with the mRNA expressed prior to birth (Kanaumi et al., 2008). Indeed, application of the pan-KCNQ blockers XE991 or linopirdine in brain slices from neonatal mice leads to increased excitability, providing evidence that KCNQ channel expression early in life prevents runaway excitation (Okada et al., 2003; Qiu et al., 2007). Additionally, overexpression of dominant-negative KCNQ2 channels in the brain during only the first of week of life results in seizures and premature lethality, suggesting that KCNQ2 channel expression is paramount during the neonatal period (Peters et al., 2005).

Loss-of-function KCNQ2 variants lead to severe neurodevelopmental disorders that present soon after birth. However, the manner in which KCNQ2 dysfunction alters cellular and network excitability early in development is currently unknown. Importantly,

eNeuro Accepted Manuscript

it remains unclear how the loss of KCNQ2 channels from excitatory neurons regulates developing hippocampal and neocortical circuits. To capture the dynamics and population activity across the forebrain in the presence and absence of KCNQ2 channels from excitatory neurons, we applied wide-field mesoscale calcium imaging from *Kcnq2* conditional knockout mice (*Pyr:Kcnq2*) and compared them with constitutive *Kcnq3* knockout mice. This approach allowed us to image the network dynamics of different forebrain circuits. We found that deletion of *Kcnq2* or *Kcnq3* resulted in multifocal and time-varying excitation across the forebrain. The spontaneous neuronal activity detected in *Pyr:Kcnq2* slices was limited by ongoing GABAA receptor activity and amplified by fast glutamatergic transmission. Importantly, in slices from *Pyr:Kcnq2* mice low-frequency activity persisted in the absence of fast synaptic transmission in the neocortex, unlike in slices from control or *Kcnq3*-null mice. Thus, ablation of *Kcnq2* channels from excitatory neurons leads to distinct aberrant activity with a unique pharmacological profile.

MATERIALS AND METHODS

Animals. All experiments were performed according to the guidelines described in the National Institutes of Health Guide for the Care and Use of Laboratory Animals and were approved by the Institutional Animal Care and Use Committee of the University of Connecticut, Storrs.

All experimental procedures were performed on mice kept under a 14-10 day-night cycle with access to food and water ad libitum. *Kcnq2*$^{f/f}$ mice on a C57BL/6J

eNeuro Accepted Manuscript

background were previously developed and described by our group and others (Soh et al., 2014; Carver and Shapiro, 2019). In the presence of Cre recombinase, exons 2-4 of the *Kcnq2*$^{f/f}$ mice are excised, leading to a premature stop codon and a non-functional protein. C57BL/6J (RRID:IMSR_JAX:000664), B6;129S6-*Polr2a*$^{Tn(pb\text{-}CAG\text{-}GCaMP5g,\text{-}tdTomato)Tvrd}$/J (RRID:IMSR_JAX:024477| PC-G5-tdT), and B6.129S2-*Emx1*$^{tm1(cre)Krj}$/J (RRID:IMSR_JAX:005628| Emx1-Cre), were purchased from the Jackson Laboratory. Breeding was performed in-house at the University of Connecticut. For this study, we bred and developed *Emx1-cre::PC-G5-tdT::Kcnq2*$^{f/+}$ mice. We intercrossed these mice to obtain *Emx1-cre::PC-G5-tdT::Kcnq2*$^{+/+}$, *Emx1-cre::PC-G5-tdT::Kcnq2*$^{f/+}$, and *Emx1-cre::PC-G5-tdT::Kcnq2*$^{f/f}$ mice. For our experiments, we used either *Emx1-cre::PC-G5-tdT::Kcnq2*$^{+/+}$ or *Emx1-cre::PC-G5-tdT::Kcnq2*$^{f/f}$ mice. td-Tomato was used to verify that Cre expression was restricted to the forebrain. Annually we refresh the Cre-deleter line by purchasing new Emx1-cre breeding pairs and breeding them with a new set of mice carrying *Kcnq2*$^{f/f}$ and PC-G5-tdT. For *Emx1-cre::PC-G5-tdT::Kcnq3*$^{-/-}$ we followed a similar strategy as with *Emx1-cre::PC-G5-tdT::Kcnq2*$^{f/f}$ line. *Kcnq3*$^{-/-}$ mice were kept on a C57BL/6J background. Genotypes were confirmed with PCR. Experiments were performed on mice of either sex.

Acute slice preparation. Mice between postnatal day 4 and 7 (P4 and P7) were brought from the vivarium into a designated area of the laboratory. Mice were then anesthetized using isoflurane. After verifying the mice were fully anesthetized, we rapidly decapitated them. Then, we placed the brains in ice-cold cutting solution containing: 26 mM $NaHCO_3$, 210 mM sucrose, 10 mM glucose, 2.5 mM KCl, 1.25 mM NaH_2PO_4, 0.5

eNeuro Accepted Manuscript

184 mM $CaCl_2$, and 7 mM $MgCl_2$. We mounted the brains on a vibratome (Leica, VS2000)
185 and prepared 300 µm horizontal slices. Slices were then placed in a 35-37°C holding
186 chamber for 30 minutes, and then moved to room temperature. The holding solution,
187 which was the same as the recording solutions for the imaging and electrophysiological
188 experiments, contained: 125 mM NaCl, 26 mM $NaHCO_3$, 2.5 mM KCl, 1 mM NaH_2PO_4,
189 1.3 mM $MgCl_2$, 1.5 mM $CaCl_2$, and 12 mM D-glucose; 32-34°C, ~310 mOsm. Slices
190 were left to rest at room temperature for at least 1 hour prior to experiments. All
191 solutions were continuously bubbled with 5% CO_2/95% O_2. The slicing procedure was
192 the same for whole-cell patch-clamp electrophysiology and calcium sensor imaging.
193
194 Whole-cell patch-clamp electrophysiology. For electrophysiological recordings, we used
195 an upright BX-51W Olympus microscope (Olympus, USA). Neurons were visualized
196 using the built-in Olympus microscope Nomarski optics, allowing for differential
197 interference contrast. We recorded from pyramidal neurons of the CA3 region of the
198 hippocampus. For current-clamp recordings we used borosilicate glass capillaries (WPI,
199 TW150F-3). The pipette resistance was 3-4 MΩ when filled with a solution containing:
200 130 mM potassium methylsulfate, 10 mM KCl, 4 mM NaCl, 4 mM Mg·ATP, 0.4 mM
201 Na_4·GTP, 10 mM HEPES, and 5 mM Tris-phosphocreatine (osmolarity ~300-310
202 mOsm). The pH was adjusted to 7.2-7.3 with KOH. Data were not corrected for the
203 junction potential. All electrophysiological data were acquired using Multiclamp 700B
204 amplifiers (Molecular Devices; RRID:SCR_018455) under the control of Clampex 10
205 software (Molecular Devices; RRID:SCR_011323). Data were acquired at 50 kHz and

eNeuro Accepted Manuscript

low-pass filtered at 10 kHz. For current-clamp recordings, the bridge balance circuit built into the Multiclamp 700B was engaged to correct for series resistance.

Imaging acute slices. Optical imaging was performed on a Zeiss Axiozoom V.16 (Zeiss) using a PlanNeoFluar Z 1x, 0.25 NA objective with a 56 mm working distance. Images were recorded using an sCMOS camera (pco.edge 4.2) at a 500×500 pixel resolution. Image acquisition was performed using Micro-Manager 2.0 beta (https://micro-manager.org/). Slices were submerged in a Warner chamber continuously perfused with extracellular solution (32-34^{o}C).

ΔF/F calculations for two-dimensional (2D) plots. We acquired and imported 300 s sCMOS sensor-recorded fluorescence time series (sampling rate: F_s=20 frames/s, 6,000 frames/recording) in MATLAB (rel. 2019b, Natick, MA; RRID:SCR_001622). Frames (500×500 pixels, inter-pixel distance: 6 μm) were inspected for the external edges of the area covered by each hemisphere, and only pixels within the area delineated by these lines were further considered. Pixels within this area were divided into *N* regions of interests (ROIs) using a simple linear iterative clustering (SLIC) algorithm (Achanta et al., 2012) (MATLAB routine: ***`superpixels`***). The SLIC algorithm was applied to the first frame of each imported time series after foreground saturation to minimize the effects of spurious calcium activity at the beginning of the time series, and the value *N* was optimized by the algorithm using an unsupervised strategy. This resulted in ROIs that were spatially homogeneous, with pixels in each ROI showing similar fluorescence intensities. For any ROI n (n =1, 2, …, *N*) and frame k (i.e., k =1,

eNeuro Accepted Manuscript

229 2, 3, …, 6,000), the ROI intensity, $F_n(k)$, was estimated as the average value of the
230 fluorescence intensity across all pixels in the ROI, and the series of variations in
231 fluorescence intensity, $\Delta F_n/F$, was estimated according to the formula:

$$\frac{\Delta F_n}{F}(k) \triangleq \frac{F_n(k) - \bar{F}(n,k)}{\bar{F}(n,k)}, \quad (1)$$

232 where $\bar{F}(n,k)$ is the average value of $F_n(k)$ over a 30-s window centered on frame k. To
233 ensure that $\bar{F}(n,k)$ captures the baseline background in the presence of sparse
234 pulsatile activity, the computation of $\bar{F}(n,k)$ was as in (Sood et al., 2019) and excluded
235 values of $F_n(k)$ in the window above the 80th percentile. ROIs were numbered
236 consecutively along the anteroposterior direction.
237
238 Time-frequency analysis. A continuous wavelet transform was applied to every $\Delta F_n/F$
239 time series (analytic Morlet wavelet, 10 voices per octave), and the resultant
240 scalograms $\mathcal{S}_n(f,k)$ were used to detect transient and sustained oscillations in the
241 ROIs. First, for any ROI n, the combinations (f,k) of frequency f and frame k at which
242 the magnitude $|\mathcal{S}_n(f,k)|$ was above a threshold T_1 identified *transient* oscillations (i.e.,
243 occurring at frame k) with period $1/f$ in the ROI. Second, for any ROI n, the cumulative
244 magnitude $\bar{\mathcal{S}}_n(f) = \sum_k |\mathcal{S}_n(f,k)|$ was computed at all frequencies f, and the values f^* at
245 which $\bar{\mathcal{S}}_n(f^*)$ was maximum and exceeded a threshold T_2 identified the presence of
246 *sustained* activity (i.e., throughout the entire time series) at frequencies f^* in the ROI.
247 Threshold T_1 was set as the 95th percentile of the values $|\mathcal{S}_n(f,k)|$ computed across all
248 frequencies f, frames k, and ROIs n, and aimed to isolate the most prominent transient
249 oscillations throughout the acute slice. Threshold T_2 was set as the 95th percentile of the

eNeuro Accepted Manuscript

values $\bar{\delta}_n(f)$ across all frequencies f and ROIs n. The combination of conditions (i) $\bar{\delta}_n(f^*) \geq \bar{\delta}_n(f)$ for all f and (ii) $\bar{\delta}_n(f^*) > T_2$ guaranteed that only the most prominent sustained oscillations throughout the slice were retained.

Finally, the cumulative spectral content of every time series $\Delta F_n/F$ was computed in two separate frequency bands, i.e., 0.02-0.2 Hz (low-frequency band, LF) and 0.2-2.0 Hz (high-frequency band, HF). The spectral content, $\mathcal{P}_B(n)$, of the series $\Delta F_n/F$ in the frequency band B ($B = LF, HF$) was computed as the integral of $|\mathcal{S}_n(f,k)|$ over B and the number of frames, i.e.:

$$\mathcal{P}_B(n) = \frac{1}{F_S} \sum_k \int_B |\mathcal{S}_n(f,k)| df \,. \qquad (2)$$

<u>ΔF/F calculations for pulse detection and measurements of amplitude and duration.</u>

ROIs exhibiting a pulsatile behavior were identified as follows. First, for any ROI n, the normalized series $\Delta F_n/F$ was evaluated for skewness (kurtosis value $K \geq 4$). If a series met the criteria for skewness, candidate peaks were selected by isolating local maxima with a minimum inter-peak distance of 30 frames. Then, for each candidate peak, three measures were computed, i.e., peak prominence, peak width w, and root mean square (RMS) in the interval of length $2w$ centered on the peak. Candidate peaks were rejected if the prominence was lower than 3.5 or the RMS was lower than 2. Threshold values on prominence, RMS, and inter-peak distance were determined offline based on the morphology and signal-to-noise ratio of the pulses in a sample series $\Delta F_n/F$. Finally, an ROI captured pulsatile activity if the corresponding time series $\Delta F_n/F$ retained three or more peaks after rejection. For ΔF/F measurements of amplitude, duration, and

eNeuro Accepted Manuscript

events/s, we used image files containing all 6,000 frames imported to Fiji-ImageJ (https://imagej.net/Fiji; RRID:SCR_002285). To determine the ΔF/F for the anatomical regions representing the CA3 area of the hippocampus or the posterior, medial, or anterior cortex, we measured the fluorescence values by drawing a shell around these areas. Fluorescence data were then extracted using the image-stack-plot z built-in Fiji function. The data were then imported to AxoGraph ver. 1.7.5 (https://axograph.com/; RRID:SCR_014284) for automated event detection. The fluorescence changes (ΔF/F) were calculated by subtracting each data point from the mean of the baseline fluorescence values. ΔF/F amplitude (calcium events with amplitude ΔF/F>0.01 were identified as events) and duration (50% of the event peak width) were analyzed using detection algorithms implemented in AxoGraph.

Determination of wave propagation velocity. To assess the propagation of oscillations across the different ROIs, we tracked the migration of calcium waves through the fluorescence time series in each hemisphere. Specifically, for every time series $\Delta F_n/F$, we computed the envelope (i.e., absolute value of the analytic signal obtained via Hilbert transform) and retrieved the envelope's highest peak, p_n^*. Then, we retained only those ROIs that (i) had a peak p_n^* with prominence greater than 3.5 and (ii) presented a *sustained* oscillation, i.e., an oscillation with frequency f^* as defined in the section '*Time-frequency analysis*' above. Finally, the retained ROIs were sorted according to the arrival time, t_n^*, of p_n^*, and the propagation velocity was estimated for consecutive ROIs. Namely, denoted with i_1, i_2, i_3,…, the ROIs after sorting, we measured the propagation velocity between ROIs i_1 and i_2, ROIs i_2 and i_3, etc., according to the

eNeuro Accepted Manuscript

formula:

$$v_j = \frac{\left\| C_{i_j} - C_{i_{j+1}} \right\|}{t^*_{i_{j+1}} - t^*_{i_j}} \quad (3)$$

where v_j denotes the velocity in propagating from ROI i_j (j =1, 2, 3, …) to the next, C_{i_j} is the centroid of the ROI i_j, and ‖·‖ denotes the Euclidian distance.

For each slice, the propagation velocity was reported as the average v_j (mean ± S.D.) across the pairs of consecutive ROIs. If less than 7 values v_j (i.e., 8 ROIs) contributed to the propagation velocity, the slice was deemed not showing oscillatory activity, and no propagation velocity was computed. Also, if two or more ROIs had their peak p^*_n arriving at the same time t^*_n, it was concluded that the ROIs were part of the same wavefront. Accordingly, the ROIs were preemptively combined into one region, and the average distance between the centroids of these ROIs and the centroid of the next ROI in the sequence was used in formula (3). The use of the Hilbert-transform and the signal envelope aimed to reduce the impact of noise on the time series and better capture the peak of the normalized fluorescence intensity, which was used as a proxy for a traveling wavefront. Also, the ROI aggregation and sorting procedures described above aimed to capture the spatial migration of a traveling wave.

Local field potential recordings. Local field potential (LFP) recordings were taken in parallel with the imaging sessions. LFPs were recorded using an RHD2000 multi-channel amplifier (Intan Technologies, Los Angeles, CA) acquired with RHD2000 interface software (ver. 1.5, copyright Intan Technologies). LFP recordings were

eNeuro Accepted Manuscript

acquired at 20 kHz, low-pass filtered (8th order Chebyshev Type I IIR filter with cutoff frequency at 80 Hz and zero-phase distortion), and downsampled to 200 Hz. The resultant LFP time series was normalized by removing the linear trend and dividing by the standard deviation, and the time-frequency analysis of the normalized LFP time series was conducted via a continuous wavelet transform as described above for $\Delta F_n/F$.

Statistics. Statistical analyses were performed using GraphPad Prism 8 software (GraphPad, San Diego, CA; RRID:SCR_002798). Summary data are expressed as bar graphs, box plots, or violin plots. Box plots show the interquartile range extending from the 25th and 75th percentiles, whereas the box plot whiskers illustrate the minimum and maximum values. We used box plots to summarize the distribution of the results and to allow the reader to quickly compare data between conditions. Violin plots allow better visualization of the distribution of the data points than box plots; thus, we used violin plots to demonstrate the full effect of the loss of *Kcnq2* or *Kcnq3* on the amplitude, duration, and events/s of the calcium responses in Figure 2 and Figure 10, respectively. For analysis, we used unpaired or paired Student's t-tests, Mann-Whitney U non-parametric unpaired tests, or Wilcoxon paired tests. Non-parametric tests were used for datasets in which the distribution of the data failed normality tests.

RESULTS

KCNQ2 channels are expressed in neonatal excitatory neurons; however, it is currently unknown how KCNQ2 dysfunction alters forebrain network excitability early in development. To address this question, we investigated the role of KCNQ2 channels in

eNeuro Accepted Manuscript

controlling excitatory neural activity in developing neurons using *Kcnq2* conditional knockout mice. To define the spatial and temporal pattern of excitatory neurons in acute slices and across the neocortex, we generated *Emx1^{cre}::PC-G5-tdT::Kcnq2$^{f/f}$* mice, denoted hereafter as *Pyr:Kcnq2* mice. In the presence of Cre recombinase, the *Pyr:Kcnq2* mice express the genetically encoded calcium sensor GCamp5g (Gee et al., 2014), which allowed us to visualize calcium events. Additionally, these mice express td-Tomato, enabling us to determine the extent of Cre recombinase activity and specificity. To maintain the circuitry between regions, we used horizontal slices from neonatal mice (P4-P7). We focused on this developmental age range because it is a critical period for the development and maturation of synaptic connectivity, corresponding to a prenatal period in humans.

***Pyr:Kcnq2* neonatal slices exhibit increased excitability**

Figure 1A compares the widefield calcium activity in horizontal slices from control and *Pyr:Kcnq2* mice. In slices of both groups, the area covering each hemisphere was decomposed into ROIs using the SLIC clustering algorithm, which aggregates pixels in a ROI if they are spatially contiguous and of similar fluorescence intensity. In this way, ROIs were constructed as macro-areas that have similar fluorescence intensities across neighbor pixels, which assures anatomical homogeneity within each macro-area. Also, because of the intra-ROI homogeneity, the fluorescence signal was averaged across pixels in each ROI, thus reducing the effects of noise on the analysis of the fluorescence time series.

eNeuro Accepted Manuscript

The results of the ROI partition indicate that *Pyr:Kcnq2* slices and control slices had a similar number of ROIs (31 ± 0.5 ROIs, n=52 hemispheres versus 31 ± 0.5 ROIs, n=64 hemispheres; *Pyr:Kcnq2* versus control p=0.62, Student's t-test; t=0.4971, df=114) and ROIs of similar size (number of pixels per ROI: 971 ± 12 pixels, n=52 hemispheres versus 963 ± 9 pixels, n=64 hemispheres; *Pyr:Kcnq2* versus control p=0.91, t=0.4971, df=114 Student's t-test). Thus, we observed no significant anatomical or functional differences between the two groups of slices.

Previous work has shown that spontaneous neuronal activity is infrequent and primarily confined to the hippocampal formation and entorhinal cortex in neonatal slices (Garaschuk et al., 2000; Namiki et al., 2013). Indeed, during a five-minute recording from control littermate slices, we observed calcium activity in the CA3 region of the hippocampus and the posterior cortex, which primarily represented the entorhinal cortex **(Figure 1A bottom panels)**. As observed in previous studies, the activity was modest in intensity, with brief pulsatile periods and few events per second **(Figure 1B)**.

Next, we examined slices from mice lacking *Kcnq2* in excitatory cells. We note that the *Emx1-cre* mice express Cre recombinase as early as E10.5 (Gorski et al., 2002); thus, by P4, KCNQ2 levels in the majority of excitatory cells would be minimal. Consistent with this assertion, we found CA3 pyramidal neurons from *Pyr:Kcnq2* mice fired a greater number of action potentials following depolarizing current injections **(Figure 1C).** Furthermore, in the absence of *Kcnq2*, calcium responses remained confined to the same pacemaker regions as in slices from control littermate mice, i.e., the CA3 region of

eNeuro Accepted Manuscript

the hippocampus and the posterior cortex **(Figure 1A)**. However, due to the loss of *Kcnq2*, the number of events during the recording period was significantly higher in both regions **(Figure 1B;** 0.012 to 0.015 events/s; ~4-5 events in 5 minutes). In addition to identifying changes in the number of detected events, we found that the duration but not amplitude of the calcium events in the posterior cortex was greater in the knockout mice **(Figure 1B;** control: 0.073 ± 0.014 ΔF/F, n=14 hemispheres; *Pyr:Kcnq2*: 0.016 ± 0.03 ΔF/F, n=20 hemispheres; p=0.08 Mann-Whitney U test). By contrast, we observed no changes in the amplitude or duration of the calcium signal for the CA3 region of the hippocampus (**Figure 1B**; control: 0.031 ± 0.006 ΔF/F, n=9 hemispheres; *Pyr:Kcnq2*: 0.034 ± 0.005 ΔF/F, n=18 hemispheres; p=0.97 Mann-Whitney U test). The observed differences between the CA3 region of the hippocampus and the posterior cortex suggested that deletion of *Kcnq2* manifests in a distinct manner in different macro-circuits.

As with the slices from control animals, we did not detect any consistent large calcium transients during the five-minute recording window in the neocortex. Similarly, earlier work showed that overall cortical activity in acute slices is very low at this developmental time point (Garaschuk et al., 2000). We note that our fluorescence signal represented calcium activity across all neuronal subcompartments; thus, at this resolution, we could not determine whether the changes in calcium signals were due to increased excitability at dendrites, soma, or axons. These changes were most likely due to a combination of all three subcompartments, as KCNQ2 channels are not simply restricted to axons in the early developmental period.

eNeuro Accepted Manuscript

To further probe the effects of *Kcnq2* deletion from the neocortex under more excitable conditions, we imaged slices that had been incubated with 8 mM extracellular potassium (Ko) for ~20 min. The use of 8 mM Ko allowed us to compare the activity of different regions under constant stimulation conditions. A concentration of 8 mM Ko was necessary to increase the event number in our slices **(Figure 2)**. We applied 8 mM Ko to slices for no more than 20 min to prevent the slices from becoming epileptic (i.e., from exhibiting spontaneous ictal events following removal of the high-potassium solution). After incubating the slices with 8 mM Ko, we recorded five-minute time-lapse movies. To complement our calcium imaging, we also recorded LFPs from the CA3 region of the hippocampus, which allowed us to correlate calcium activity to the overall network activity. Similar to the recordings in low-potassium artificial cerebrospinal fluid, we found that the majority of calcium events in slices from control animals originated from the hippocampal formation and posterior cortex, closely following the measured LFPs **(Figure 2B; Movie 1)**.

In contrast to the control slices, slices from mice lacking KCNQ2 channels exhibited widespread calcium activity spanning all cortical regions and layers (**Figure 2** and **Movie 2).** Closer examination of the time-lapse movies also showed that activity in the neocortex frequently initiated in the upper cortical layers and then migrated to the deeper layers and neighboring neocortical regions (**see movie 2)**. Calcium waves propagated in multiple directions and were generally multifocal, as the initial activity sprang at multiple regions. We also found that the calcium events were larger and

eNeuro Accepted Manuscript

longer lasting across all regions **(Figure 2C)**. Additionally, the average propagation velocity of the calcium responses across ROIs in slices from *Pyr:Kcnq2* mice was 0.64 ± 0.074 mm/s (n=55 hemispheres), which was almost three times slower than the rate measured in control slices (2.07 ± 0.53 mm/s, n=18 hemispheres, p=0.0006 Mann-Whitney U test). We currently do not know the reason for this difference, but there could be many contributing factors such as the location of the calcium signal, or the presence of multiple waves with different latencies instead of one large, synchronous wave. We did not investigate this further.

Although the calcium activity was robust in CA3, we noticed that the LFPs were typically smaller or absent in slices from *Pyr:Kcnq2* mice. This result could be attributed to several reasons, such as electrode placement, increased gamma-aminobutyric acid (GABA)-ergic receptor activity (see below), the higher tendency of *Kcnq2*-null excitatory neurons to show spreading depression and persistent depolarization leading to sodium channel inactivation (Aiba and Noebels, 2020), or a combination of these mechanisms. We did not pursue this question further. Importantly, independent of the region being imaged, we observed an increase in both the amplitude and duration of calcium events **(Figure 2C)**. This trend was particularly striking in the medial and anterior cortex, where the event amplitude increased by ~50 fold (i.e., medial cortex: from 0.02 $\Delta F/F$ to 0.33 $\Delta F/F$).

In slices from *Pyr:Kcnq2* mice, large calcium events in CA3 and the posterior cortex were organized in low-frequency patterns. Additionally, the average number of events in

eNeuro Accepted Manuscript

the calcium fluorescence signals in both regions was decreased compared to the number of events from control slices (CA3, decreased from 0.025 to 0.004 events/s; posterior cortex, decreased from 0.013 to 0.005 events/s) **(Figure 2C)**. This shift in the number of events reflects the loss of small events and the emergence of longer-lasting less frequent large population events. Indeed, the duration of average calcium events increased from 1.4 s to 8.5 s and 2.2 s to 6.5 s in the CA3 region of the hippocampus and the posterior cortex, respectively. In contrast, in the medial and anterior cortex, we primarily observed an increase rather than a decrease in the number of calcium events (medial cortex: 0.006 events/s to 0.018 events/s; anterior cortex: 0.012 events/s to 0.021 events/s) **(Figure 2C)**, which primarily reflects the appearance of prolonged synchronous activity following the large depolarization of the posterior cortex and the CA3 region of the hippocampus. Thus, based on these data, we conclude that the loss of *Kcnq2* from excitatory neurons increases excitability, manifested as large population events, across the forebrain, independent of the region. This trend is consistent with the wide distribution of KCNQ2 channels in the forebrain (Cooper et al., 2001).

Kcnq2 deletion leads to transient slow-wave patterns

To further quantify the effects of *Kcnq2* deletion on the calcium signals from excitatory cells, we conducted a time-frequency analysis of the fluorescence time series **(Figure 3)** and measured the cumulative magnitude of these signals in the low-frequency (LF; 0.02-0.2 Hz) and high-frequency (HF; 0.2-2 Hz) bands, which captured the majority of the activity in our slices. **Figure 3A** shows the time-frequency analysis averaged across all ROIs and indicates that the loss of *Kcnq2* primarily increased activity in the LF band.

eNeuro Accepted Manuscript

476 Moreover, the left panels of **Figure 3B** show the sample distribution of the frequency f
477 of the transient oscillations across all ROIs for *Kcnq2* (red line) and control (black line),
478 respectively, whereas the right panels report the number of ROIs that exhibited
479 sustained oscillations (i.e., a histogram of frequencies f^*). All panels refer to the slices
480 in **Figure 2A**. Together, **Figures 3A** and **3B** show that deleting *Kcnq2* is associated
481 with widespread oscillations at frequencies concentrated in the LF band. This result was
482 confirmed at the population-level, i.e., we reported that, across all slices, the oscillations
483 spanned a larger number of ROIs in *Pyr:Kcnq2* slices than control slices (**Figure 3C-D**),
484 were sustained throughout the duration of the recording period, and exhibited transient
485 modulations of the fundamental frequency, although the fundamental frequency
486 remained primarily confined to the LF band (**Figure 3C-D**). In contrast, few ROIs
487 showed significant periodic oscillations in the HF range, as summarized in **Figure 3D**.
488
489 Together, these findings are consistent with our earlier observation that loss of *Kcnq2*
490 primarily leads to the appearance of large but less frequent population events (see
491 **Figure 2**). However, these data also show that deletion of *Kcnq2* from forebrain
492 excitatory neurons leads to multiple hot spots at low frequencies in the presence of
493 elevated extracellular potassium. These hot spots are distributed across the entire slice
494 and can be spatially separated but retain similar frequencies, which strongly indicates
495 that the hot spots could stem from increased network signaling.
496
497 **GABAA receptor activity amplifies without shaping *Kcnq2* slow-wave patterns**
498 To further understand the role of network signaling in the formation of low-frequency hot

eNeuro Accepted Manuscript

spots, we conducted follow-up experiments to determine whether these slow oscillations are driven by glutamatergic or GABAergic activity. **Figure 4** shows that inhibition of GABAA receptors using 50 µM picrotoxin (PTX), a ubiquitous GABAA receptor open channel antagonist that blocks both synaptic and extra-synaptic GABAA receptors, further exacerbated the increase in network activity in both control and *Pyr:Kcnq2* slices **(Figure 4A-B).** Picrotoxin also sped up, almost doubling, the propagation velocity of the calcium activity in *Pyr:Kcnq2* slices (from 0.59 ± 0.11 to 1.08 ± 0.15 mm/s, n=20 hemispheres, p=0.0136 Wilcoxon pair test), further suggesting that GABAA receptors limit the spread of calcium responses in the forebrain. Our results are consistent with several studies showing that the application of PTX can increase network activity in the neonatal brain, even when GABA acts as an excitatory transmitter due to its depolarized chloride equilibrium potential in neonatal excitatory neurons [e.g., (Kirmse et al., 2015; Che et al., 2018); but also see (Murata and Colonnese, 2020)]. Independent of the genotype, blocking GABAA receptors led to larger fluorescence signal amplitudes in all areas of the forebrain (**Figure 4B-C**). However, the average calcium event duration decreased as blocking GABAA receptors led to the appearance of larger but briefer calcium signals in the *Pyr:Kcnq2* slices (**Figure 4B-C**). We also observed this trend in the LFP recordings (**Figure 4B**), suggesting that GABAA receptor activation dampens ongoing network activity in the absence of *Kcnq2* across the forebrain. Consistent with uniform upregulation of activity in slices from *Pyr:Kcnq2* mice, we found a generalized increment of the time-frequency signal in response to PTX independent of the genotype **(Figure 5A)**. This resulted in a significant increase of the power both in the LF and HF bands at the population-level (i.e., across slices), and the percent increase in power

eNeuro Accepted Manuscript

with respect to the pre-PTX case was similar in slices from *Pyr:Kcnq2* and control mice. Vice versa, the probability density of the frequency f of transient oscillations in a slice (**Figure 5B-C**) and the total number (i.e., across all slices) of ROIs exhibiting a sustained oscillation (**Figure 5D**) were similar before and after applying PTX, which indicates that the temporal pattern of neural activity was not altered by PTX. Moreover, no ROIs in slices from *Pyr:Kcnq2* mice exhibited sustained oscillations in the HF band, and this trend remained unaffected by the application of PTX (**Figure 5D**).

Combined, **Figure 4** and **Figure 5** indicate that PTX increases the energy of the fluorescence signals from each ROI without altering the temporal pattern of the activity, both in slices from *Pyr:Kcnq2* and control mice. This finding suggests that the application of PTX facilitates the synchronization among neurons within each ROI (i.e., local microcircuits) but has limited impact on the recruitment of distinct ROIs into a common pattern. It also suggests that the shift in behavior observed in slices from *Pyr:Kcnq2* mice is not affected by local synaptic GABAergic transmission but rather stems from a change in neural excitability throughout the forebrain.

N-methyl-d-aspartate (NMDA) receptor inhibition attenuates *Kcnq2* slow-wave patterns

We then assessed whether the low-frequency activity observed in slices from *Pyr:Kcnq2* mice depends on glutamatergic activity. Previous work has shown that in the presence of 8 mM Ko, increased network excitability is partly driven by the activation of NMDA glutamate receptors (Traynelis and Dingledine, 1988). This phenomenon occurs

eNeuro Accepted Manuscript

because NMDA receptors have slow deactivation kinetics, which allows for prolonged dendritic depolarization, leads to a downstream increase in somatic and axonal excitability, and causes a buildup of extracellular potassium.

Consistent with this model, application of 25 μM D-APV (D-2-Amino-5-phosphonovalerate) to our control slices reduced the amplitude of the calcium signals across all regions by approximately 50-100% with the smallest effect at the CA3 region and the largest at the medial cortex **(Figure 6)**, thus suggesting that NMDA receptor activity is a key driver of network excitability in control slices. In contrast, inhibition of NMDA receptors had more complex effects in slices from *Pyr:Kcnq2* mice. First, blocking NMDA receptors reduced calcium activity by ~30-50% in all forebrain regions **(Figure 6B-C)**. Second, blocking NMDA receptors prolonged the duration of calcium signals across all regions **(Figure 6C)**. This was due to the fact that NMDA receptor inhibition primarily targets large, faster events, causing the average signals to be mediated by longer lasting synchronous events **(Figure 6C)**. Accordingly, the time-frequency signal was significantly attenuated by application of APV **(Figure 7A)** and resulted in a significant attenuation (i.e., 20-30%) of the power content both at LF and HF values **(Figure 7C)**. However, the application of APV did not alter substantially the sample distribution of transient oscillation frequencies **(Figure 7B)** or the number of ROIs with significant sustained oscillations **(Figure 7D)**. Altogether, the behavior described in **Figure 6** and **Figure 7** is in contrast to the effect induced by blocking GABAA receptors and suggests that ongoing population network activity in *Kcnq2*-null excitatory neurons partially requires NMDA receptors. Furthermore, these results

eNeuro Accepted Manuscript

suggest that, in *Pyr:Kcnq2* slices, NMDA receptor inhibition primarily reduces the overall activity without necessarily suppressing large calcium events.

Fast synaptic transmission does not prevent slow waves in slices from *Pyr:Kcnq2* mice.

To clarify whether the modulatory behavior reported above is restricted to NMDA receptors or rather extends to rapid synaptic transmission in general, we imaged control and *Pyr:Kcnq2* slices in the presence of the rapid synaptic transmission blockers NBQX (2,3-dioxo-6-nitro-7-sulfamoyl-benzo[f]quinoxaline, AMPA receptor blocker), D-APV (NMDA receptor blocker), and PTX (GABAA receptor blocker). We found that blocking all fast synaptic transmission entirely abolished calcium activity in control slices **(Figure 8A-B)**, as reported previously (Sipila et al., 2005; Sheroziya et al., 2009). In contrast, in *Pyr:Kcnq2* slices activity was reduced across the forebrain, but still persisted significantly **(Figure 8B, Movie 3)**. In particular, we found a substantial reduction in pulsatile events of smaller amplitude and higher frequency, while large-amplitude calcium population events remained intact. Because of this, we observed an increase in the amplitude (posterior and medial cortex) and duration (CA3 region of the hippocampus, posterior and anterior cortex) **(Figure 8B, see Table 1 for data summary)**. We note that the observed increases in duration and average amplitude were primarily due to the loss of small and short-lasting events; thus, the average duration was enriched by the long-lasting high-amplitude calcium events, rather than the emergence of new larger calcium events. We also did not find any effect of fast synaptic blockers on the propagation velocity of the calcium events (0.59 ± 0.11 mm/s, n=20

eNeuro Accepted Manuscript

591 hemispheres; 0.69 ± 0.13 mm/s, n=18, p=0.74 Mann-Whitney U test). In contrast to the
592 experiments using fast synaptic blockers, calcium responses were eliminated upon
593 application of 1 μM tetrodotoxin (TTX) **(Figure 8C)**, suggesting that voltage-gated
594 sodium channel activity was required for the aberrant calcium responses in *Pyr:Kcnq2*
595 slices.
596
597 Similar to the data in **Figure 8**, we observed no significant changes in the time-
598 frequency patterns in the *Pyr:Kcnq2* slices upon suppression of fast synaptic
599 transmission, i.e., the suppression failed to evoke substantial changes in the frequency
600 distribution of transient oscillations across ROIs **(Figure 9A-B)** or the number of ROIs
601 that exhibited sustained oscillations **(Figure 9D)**. Instead, blocking fast synaptic
602 transmission lowered the overall intensity of the transient oscillations **(Figure 9A)** and
603 resulted in lower spectral content in both the LF and HF bands **(Figure 9C)**. Finally, we
604 did not observe these effects in the control slices; instead and in line with the
605 expectations of blocking synaptic transmission, we found a robust suppression of
606 transient oscillations across all ROIs **(Figure 9B)** and a large reduction in the number of
607 ROIs exhibiting sustained oscillations **(Figure 9D)**. Together, these data suggest that
608 loss of KCNQ2 channels drives low-frequency activity through a mechanism that is
609 independent of fast synaptic transmission. Thus, in the absence of rapid synaptic
610 transmission, slices from *Pyr:Kcnq2* mice can still generate large hypersynchronous
611 events, likely due to sodium channel-driven depolarization of *Kcnq2*-null excitatory
612 neurons and a large build-up and diffusion of potassium (Aiba and Noebels, 2020).
613

eNeuro Accepted Manuscript

Effects of *Kcnq3* deletion on network activity

Recent work has shown that KCNQ3 dysfunction leads to pharmacodependent epilepsy in patients lacking both functional *Kcnq3* copies (Lauritano et al., 2019), which is distinct from the pharmacoresistant epilepsy caused by KCNQ2 dominant-negative variants (Cornet et al., 2018). Hence, we investigated whether loss of KCNQ3 activity leads to similar or different slow hypersynchronous events in the forebrain compared to loss of KCNQ2 activity. We thus repeated our experiments in *Kcnq3*-knockout mice crossed with *Emx1^{cre}:PC:Gcamp5*, as *Kcnq3$^{-/-}$* mice survive to adulthood.

The activity in the *Kcnq3*-null slices was qualitatively similar to that in the slices without *Kcnq2*. Thus, ablation of *Kcnq3* also increases the network excitability across the forebrain and can lead to the emergence of large low-frequency propagation calcium events (*Kcnq3$^{-/-}$* calcium propagation velocity = 0.73 ± 0.15 mm/s, n=20 hemispheres) **(Figure 10; Movie 4)**, thus suggesting a previously unappreciated role of KCNQ3 channels in the neonatal forebrain. However, we note several similarities and differences between the two mouse lines: (i) Unlike in *Pyr:Kcnq2* mice, ablation of *Kcnq3* did not increase the amplitude or the duration of calcium signals across all areas **(Figure 10B-C)**. For instance, we primarily found increases in the posterior cortex with less of an effect in the CA3 region of the hippocampus. (ii) We observed an increase in the probability density, power, and ROIs primarily at the low-frequency domain in *Kcnq3$^{-/-}$* slices. However, the overall increases were smaller than we observed in the *Pyr:Kcnq2* slices **(Figure 11 compared to Figure 3)**. This smaller change in excitability due to *Kcnq3* ablation is consistent with the less severe phenotypes of *Kcnq3*- than

eNeuro Accepted Manuscript

637 *Kcnq2*-deficient mice (Soh et al., 2014).

638

639 Next, we tested whether the increase in low-frequency calcium events in *Kcnq3*-
640 knockout mice is dependent on fast synaptic transmission. We found that the
641 neocortical activity in *Kcnq3*-null mice was fully dependent on fast glutamatergic
642 transmission, as co-application of NBQX and APV in the presence of PTX eliminated all
643 ongoing activity at the neocortex **(Figure 12**); this effect was not observed with
644 *Pyr:Kcnq2* mice but was similar to what we found in control slices. Consequently, we
645 found an overall decrease in the power and ROIs in slices from either $Kcnq3^{+/+}$ or
646 $Kcnq3^{-/-}$ slices **(Figure 13)**. Importantly, glutamatergic activity did not block the low-
647 frequency calcium events in the hippocampus similar to what we found in slices from
648 *Pyr:Kcnq2* mice. This is best illustrated in **Figure 13**. Thus, KCNQ2 and KCNQ3 loss
649 could lead to the generation of low-frequency hypersynchronous events, but their
650 dependence on fast synaptic transmission is specific to the forebrain region (see
651 discussion below).

652

653 **DISCUSSION**

654 In this work, we determined the role of KCNQ2 and KCNQ3 channels in regulating the
655 network activity of forebrain neonatal neuronal circuits. Although KCNQ2 and KCNQ3
656 channels are expressed in both GABAergic and glutamatergic neurons (Cooper et al.,
657 2001), we primarily focused on forebrain excitatory cells as KCNQ2/3 channels regulate
658 multiple facets of their excitability. The key findings of our study are that (i) KCNQ2
659 channel loss from pyramidal neurons can lead to multifocal spreading activity across all

eNeuro Accepted Manuscript

660 regions of the forebrain, (ii) large low-frequency calcium events modestly depend on
661 fast synaptic transmission, and (iii) unlike *Pyr:Kcnq2* mice, *Kcnq3*-null mice exhibit low-
662 frequency hypersynchronous activity driven by glutamatergic transmission in the
663 neocortex but not the hippocampus. Our results provide new insights into the role of
664 KCNQ2 and KCNQ3 channels in the neonatal brain and demonstrate that loss of
665 KCNQ2 channels drives hyperexcitability in a manner distinct from KCNQ3-induced
666 hypersynchrony in the neonatal neocortex.
667
668 **KCNQ2 channels in the developing forebrain**
669 KCNQ2 channels are unique as they are expressed early in development, prior to birth
670 (Kanaumi et al., 2008). For instance, studies examining KCNQ2 mRNA from human
671 brain at different gestational periods have shown that KCNQ2 mRNA is expressed as
672 early as 50 days post conception (http://development.psychencode.org/#). Consistent
673 with this, KCNQ2 protein levels are highly expressed during the perinatal and early
674 infantile period (Kanaumi et al., 2008). Thus, in retrospect it is not surprising that
675 KCNQ2 pathogenic variants lead to range of pediatric epilepsy disorders from benign
676 familial neonatal seizures to developmental and epileptic encephalopathies (Nappi et
677 al., 2020).
678
679 The critical function of KCNQ2 channels early in development has also been supported
680 in work with certain mouse models. For instance, loss-of-function *Kcnq2* homozygous
681 mice die within one hour following birth (Watanabe et al., 2000). Additionally,
682 overexpression of dominant-negative isoforms of KCNQ2 channels during the first week

eNeuro Accepted Manuscript

683 of life, but not later, leads to lifelong seizures and premature death (Peters et al., 2005).
684 Our work builds on these previous findings and makes several new contributions. Until
685 now, most studies on the function of KCNQ2 channels in the developing cortex have
686 focused on the hippocampus using pan-KCNQ channel blockers like XE991 and
687 linopiridine (Okada et al., 2003; Qiu et al., 2007; Safiulina et al., 2008). However, such
688 pharmacological reagents could not distinguish between KCNQ2 and KCNQ3, or parse
689 through the contribution of different cell populations. By combining the use of *Kcnq2*
690 conditional knockout mice and mesoscale calcium imaging, we were able to define the
691 function of KCNQ2 channels from excitatory neurons in the neonatal forebrain. Although
692 activity under basal conditions was primarily confined to the hippocampus and posterior
693 cortex, application of 8 mM extracellular potassium revealed a large hyperexcitable
694 phenotype across the forebrain in slices from *Pyr:Kcnq2* animals. The activity was
695 multifocal, that is multiple regions showed large population calcium events that on
696 occasion would migrate across the neocortex. On many occasions, activity started at
697 the entorhinal cortex, which then propagated to the neocortex or hippocampus;
698 however, we also observed activity starting at the anterior cortical areas closer to the
699 medial occipital cortex. Our data are consistent with an earlier imaging study from the
700 neonatal brain that found that cortical waves typically originate from the entorhinal
701 cortex (Namiki et al., 2013). We caution that our work was performed on acute slices
702 that have many severed connections between regions; thus, in an intact brain,
703 additional regions might also be hyperexcitable in the absence of KCNQ2 channels.
704

eNeuro Accepted Manuscript

KCNQ2-containing channels have a critical role in controlling the excitability of the neonatal brain (Peters et al., 2005). Immature neurons have a depolarized membrane potential that would drive many voltage-gated potassium channels to either fast or slow inactivation, rendering them incapable of clamping down the membrane potential below the threshold to generate an action potential and preventing sodium channel inactivation (Telezhkin et al., 2018). KCNQ2 channels are slow-activating, non-inactivating potassium channels (Jentsch, 2000). Thus, KCNQ2 channels would remain open at resting membrane potentials of immature neurons (~-30 mV to -50 mV depending on the age of the neuron) preventing unwanted excitation (Telezhkin et al., 2018). Additionally, the probability of KCNQ2 opening and voltage activation mid-point is modulated by the phospholipid PIP2 (Kim et al., 2016; Greene and Hoshi, 2017). This allows neurons to tailor KCNQ2 activity by changing membrane PIP2 levels. Thus, KCNQ2 channel gating properties and the subcellular localization, which early in development is both somatic and axonal, are suited for regulating the properties of immature neurons, prior to the full expression of additional voltage-gated and leak potassium channels.

KCNQ2 versus KCNQ3 in neonatal excitability

Recent studies have shown that complete loss of KCNQ3 channel function can lead to pharmacodependent epilepsy and intellectual disability (Lauritano et al., 2019). Consistent with this, we found that loss of KCNQ3 activity leads to a hyperexcitable forebrain in the presence of an increased extracellular potassium concentration. Our data are consistent with earlier reports demonstrating mRNA expression of KCNQ3

eNeuro Accepted Manuscript

728 from early developmental points and protein expression of KCNQ3 in human patients
729 during pregestational time periods (Kanaumi et al., 2008). However, KCNQ3 loss had
730 less robust effects than loss of KCNQ2 channels from the neocortex. This difference
731 could be due to lower protein expression levels of KCNQ3 than KCNQ2 channels early
732 in development or due to the presence of KCNQ2 channels, which could still function in
733 the absence of KCNQ3 in neurons (Soh et al., 2014).
734
735 We also found that in *Kcnq3*-ablated mice, the aberrant neocortical activity was driven
736 by synaptic activity, unlike the hypersynchrony due to KCNQ2 loss, further suggesting
737 that loss of KCNQ2 or KCNQ3 lead to distinct effects in the developing brain. One
738 possibility for the difference between the *Kcnq3*- and *Kcnq2*-deficient neocortex might
739 be that *Kcnq3* was removed from both interneurons and pyramidal neurons in contrast
740 to *Kcnq2*. However, we do not think this could fully explain the difference between the
741 mouse lines as the hyperexcitability in hippocampus was insensitive to synaptic
742 transmission blockers in both *Kcnq2* and *Kcnq3* transgenic animals. Rather, the
743 differences might reflect varying KCNQ2 and KCNQ3 protein expression level among
744 the different regions early in development. Future studies are needed to decipher the
745 role of KCNQ2 and KCNQ3 channels in the neonatal brain.
746
747 **Possible model to explain our data**
748 What could drive the slow hypersynchronous events? Based on knowledge from
749 previous studies we propose the following working model. Under elevated excitability
750 conditions such as in the presence of 8 mM extracellular potassium, a concentration

eNeuro Accepted Manuscript

751 that the brain could easily reach during robust activity or seizures, *Kcnq2*-null and (to a
752 lesser extent) *Kcnq3*-null excitatory neurons would fire a barrage of action potentials or
753 drive neurons to a prolonged afterdepolarization due to unabated persistent sodium
754 channel activity. A prolonged somatic and axonal depolarization in the absence of
755 synaptic blockers might further build up extracellular potassium due to the continual
756 activation of voltage-gated potassium channels and the engagement of glutamate-gated
757 NMDA and AMPA receptors. The large build-up of potassium would diffuse across
758 neighboring regions, initiating waves of depolarization and network activity across the
759 forebrain with its scope limited by ongoing GABAA receptor activity. Further
760 experiments are needed to test the different scenarios using additional transgenic mice.
761
762 In conclusion, our study fills an important knowledge gap by showing that loss of
763 KCNQ2 and to a lesser extent KCNQ3 function from the neonatal forebrain can lead to
764 a hypersynchrony in the neonatal brain that does not fully rely on the presence of fast
765 glutamatergic transmission.
766
767 **Acknowledgements:** This work was supported by National Institutes of Health grants
768 R01 NS101596, HL137094, and NS108874 (to A.V.T.), and NSF CAREER Award
769 1845348 (to S.S.).
770
771 **REFERENCES**

772 Achanta R, Shaji A, Smith K, Lucchi A, Fua P, Susstrunk S (2012) SLIC superpixels compared
773 to state-of-the-art superpixel methods. IEEE Trans Pattern Anal Mach Intell 34:2274-2282.

774 Aiba I, Noebels JL (2020) Kcnq2/Kv7.2 controls the threshold and bihemispheric symmetry of
775 cortical spreading depolarization. bioRxiv:2020.2011.2027.401570.

eNeuro Accepted Manuscript

776 Carver CM, Shapiro MS (2019) Gq-Coupled Muscarinic Receptor Enhancement of KCNQ2/3
777 Channels and Activation of TRPC Channels in Multimodal Control of Excitability in Dentate
778 Gyrus Granule Cells. J Neurosci 39:1566-1587.

779 Che A, Babij R, Iannone AF, Fetcho RN, Ferrer M, Liston C, Fishell G, De Marco Garcia NV
780 (2018) Layer I Interneurons Sharpen Sensory Maps during Neonatal Development. Neuron
781 99:98-116 e117.

782 Cooper EC (2011) Made for "anchorin": Kv7.2/7.3 (KCNQ2/KCNQ3) channels and the
783 modulation of neuronal excitability in vertebrate axons. Semin Cell Dev Biol 22:185-192.

784 Cooper EC, Harrington E, Jan YN, Jan LY (2001) M channel KCNQ2 subunits are localized to
785 key sites for control of neuronal network oscillations and synchronization in mouse brain. J
786 Neurosci 21:9529-9540.

787 Cornet MC, Sands TT, Cilio MR (2018) Neonatal epilepsies: Clinical management. Semin Fetal
788 Neonatal Med 23:204-212.

789 Garaschuk O, Linn J, Eilers J, Konnerth A (2000) Large-scale oscillatory calcium waves in the
790 immature cortex. Nat Neurosci 3:452-459.

791 Gee JM, Smith NA, Fernandez FR, Economo MN, Brunert D, Rothermel M, Morris SC, Talbot A,
792 Palumbos S, Ichida JM, Shepherd JD, West PJ, Wachowiak M, Capecchi MR, Wilcox KS,
793 White JA, Tvrdik P (2014) Imaging activity in neurons and glia with a Polr2a-based and cre-
794 dependent GCaMP5G-IRES-tdTomato reporter mouse. Neuron 83:1058-1072.

795 Geisheker MR et al. (2017) Hotspots of missense mutation identify neurodevelopmental
796 disorder genes and functional domains. Nat Neurosci 20:1043-1051.

797 Gorski JA, Talley T, Qiu M, Puelles L, Rubenstein JL, Jones KR (2002) Cortical excitatory
798 neurons and glia, but not GABAergic neurons, are produced in the Emx1-expressing lineage.
799 J Neurosci 22:6309-6314.

800 Greene DL, Hoshi N (2017) Modulation of Kv7 channels and excitability in the brain. Cell Mol
801 Life Sci 74:495-508.

802 Jentsch TJ (2000) Neuronal KCNQ potassium channels: physiology and role in disease. Nat
803 Rev Neurosci 1:21-30.

804 Kanaumi T, Takashima S, Iwasaki H, Itoh M, Mitsudome A, Hirose S (2008) Developmental
805 changes in KCNQ2 and KCNQ3 expression in human brain: possible contribution to the age-
806 dependent etiology of benign familial neonatal convulsions. Brain Dev 30:362-369.

807 Kim KS, Duignan KM, Hawryluk JM, Soh H, Tzingounis AV (2016) The Voltage Activation of
808 Cortical KCNQ Channels Depends on Global PIP2 Levels. Biophys J 110:1089-1098.

809 Kirmse K, Kummer M, Kovalchuk Y, Witte OW, Garaschuk O, Holthoff K (2015) GABA
810 depolarizes immature neurons and inhibits network activity in the neonatal neocortex in vivo.
811 Nat Commun 6:7750.

eNeuro Accepted Manuscript

812 Lauritano A, Moutton S, Longobardi E, Tran Mau-Them F, Laudati G, Nappi P, Soldovieri MV,
813 Ambrosino P, Cataldi M, Jouan T, Lehalle D, Maurey H, Philippe C, Miceli F, Vitobello A,
814 Taglialatela M (2019) A novel homozygous KCNQ3 loss-of-function variant causes non-
815 syndromic intellectual disability and neonatal-onset pharmacodependent epilepsy. Epilepsia
816 Open 4:464-475.

817 Murata Y, Colonnese MT (2020) GABAergic interneurons excite neonatal hippocampus in vivo.
818 Sci Adv 6:eaba1430.

819 Namiki S, Norimoto H, Kobayashi C, Nakatani K, Matsuki N, Ikegaya Y (2013) Layer III neurons
820 control synchronized waves in the immature cerebral cortex. J Neurosci 33:987-1001.

821 Nappi P, Miceli F, Soldovieri MV, Ambrosino P, Barrese V, Taglialatela M (2020) Epileptic
822 channelopathies caused by neuronal Kv7 (KCNQ) channel dysfunction. Pflugers Arch
823 472:881-898.

824 Okada M, Zhu G, Hirose S, Ito KI, Murakami T, Wakui M, Kaneko S (2003) Age-dependent
825 modulation of hippocampal excitability by KCNQ-channels. Epilepsy Res 53:81-94.

826 Peters HC, Hu H, Pongs O, Storm JF, Isbrandt D (2005) Conditional transgenic suppression of
827 M channels in mouse brain reveals functions in neuronal excitability, resonance and
828 behavior. Nat Neurosci 8:51-60.

829 Qiu C, Johnson BN, Tallent MK (2007) K+ M-current regulates the transition to seizures in
830 immature and adult hippocampus. Epilepsia 48:2047-2058.

831 Safiulina VF, Zacchi P, Taglialatela M, Yaari Y, Cherubini E (2008) Low expression of Kv7/M
832 channels facilitates intrinsic and network bursting in the developing rat hippocampus. J
833 Physiol 586:5437-5453.

834 Satterstrom FK et al. (2020) Large-Scale Exome Sequencing Study Implicates Both
835 Developmental and Functional Changes in the Neurobiology of Autism. Cell 180:568-584
836 e523.

837 Sheroziya MG, von Bohlen Und Halbach O, Unsicker K, Egorov AV (2009) Spontaneous
838 bursting activity in the developing entorhinal cortex. J Neurosci 29:12131-12144.

839 Singh NA, Otto JF, Dahle EJ, Pappas C, Leslie JD, Vilaythong A, Noebels JL, White HS, Wilcox
840 KS, Leppert MF (2008) Mouse models of human KCNQ2 and KCNQ3 mutations for benign
841 familial neonatal convulsions show seizures and neuronal plasticity without synaptic
842 reorganization. J Physiol 586:3405-3423.

843 Sipila ST, Huttu K, Soltesz I, Voipio J, Kaila K (2005) Depolarizing GABA acts on intrinsically
844 bursting pyramidal neurons to drive giant depolarizing potentials in the immature
845 hippocampus. J Neurosci 25:5280-5289.

846 Soh H, Pant R, LoTurco JJ, Tzingounis AV (2014) Conditional deletions of epilepsy-associated
847 KCNQ2 and KCNQ3 channels from cerebral cortex cause differential effects on neuronal
848 excitability. J Neurosci 34:5311-5321.

eNeuro Accepted Manuscript

Soh H, Park S, Ryan K, Springer K, Maheshwari A, Tzingounis AV (2018) Deletion of KCNQ2/3 potassium channels from PV+ interneurons leads to homeostatic potentiation of excitatory transmission. Elife 7.

Sood D, Cairns DM, Dabbi JM, Ramakrishnan C, Deisseroth K, Black LD, 3rd, Santaniello S, Kaplan DL (2019) Functional maturation of human neural stem cells in a 3D bioengineered brain model enriched with fetal brain-derived matrix. Sci Rep 9:17874.

Telezhkin V, Straccia M, Yarova P, Pardo M, Yung S, Vinh NN, Hancock JM, Barriga GG, Brown DA, Rosser AE, Brown JT, Canals JM, Randall AD, Allen ND, Kemp PJ (2018) Kv7 channels are upregulated during striatal neuron development and promote maturation of human iPSC-derived neurons. Pflugers Arch 470:1359-1376.

Traynelis SF, Dingledine R (1988) Potassium-induced spontaneous electrographic seizures in the rat hippocampal slice. J Neurophysiol 59:259-276.

Verneuil J, Brocard C, Trouplin V, Villard L, Peyronnet-Roux J, Brocard F (2020) The M-current works in tandem with the persistent sodium current to set the speed of locomotion. PLoS Biol 18:e3000738.

Wang T et al. (2020) Large-scale targeted sequencing identifies risk genes for neurodevelopmental disorders. Nat Commun 11:4932.

Watanabe H, Nagata E, Kosakai A, Nakamura M, Yokoyama M, Tanaka K, Sasai H (2000) Disruption of the epilepsy KCNQ2 gene results in neural hyperexcitability. J Neurochem 75:28-33.

eNeuro Accepted Manuscript

871 **FIGURE LEGENDS**

872 **Figure 1. Ablation of *Kcnq2* from neonatal excitatory neurons leads to increased**
873 **excitability in the hippocampus and posterior cortex.** All recordings were in the
874 presence of 2.5 mM Ko. **(A)** Top panels show examples of acute slices from control and
875 *Pyr:Kcnq2* mice with one hemisphere segmented into ROIs. Bottom panels,
876 representative 2D plots showing calcium activity (ΔF/F) as a function of time for the
877 different ROIs. The numbering corresponds to the segmented area shown on the top
878 panels with lower values towards the anterior cortex (AC) and higher values towards the
879 CA3 area of the hippocampus and posterior cortex (PC). **(B)** Summary graphs show the
880 effect of *Kcnq2* ablation on the calcium event duration and frequency for the CA3 area
881 of the hippocampus and the posterior cortex. Data in the box plots show the median and
882 the interquartile range. **(C)** Whole-cell recordings from CA3 pyramidal neurons show
883 that ablation of *Kcnq2* increases neuronal excitability. Left panels, family of depolarizing
884 1 s current steps in either control or *Pyr:Kcnq2* slices. Right, summary graph shows the
885 number of recorded action potentials in control and *Pyr:Kcnq2* CA3 pyramidal neurons.
886 For (C) data are represented as mean ± s.e.m. Additional details on the statistical
887 analysis for this figure are found in Table 1 under the Figure 1 section.

888

889 **Figure 2. Deletion of *Kcnq2* from excitatory neurons leads to elevated calcium**
890 **activity across the forebrain in 8 mM Ko**. **(A)** Top panels show examples of acute
891 slices from control and *Pyr:Kcnq2* mice with one hemisphere segmented into ROIs.
892 Bottom panels, 2D plots show the calcium activity across the different ROIs. The
893 numbering corresponds to the segmented area shown on the top panels with lower
894 values towards the AC and higher values towards the PC. Note that in the absence of

eNeuro Accepted Manuscript

Kcnq2, substantial calcium activity is measured across all regions of the forebrain. **(B)** Top two panels show the temporal evolution of the LFPs and ΔF/F recorded in parallel in the CA3 region of the hippocampus. Note that in contrast to the LFPs in slices from *Pyr:Kcnq2* mice, the calcium responses are large and long-lasting. Middle and bottom panels show the temporal evolution of the ΔF/F across multiple ROIs. **(C)** Violin plots show the effect of *Kcnq2* deletion on the amplitude, duration, and frequency of the calcium events for different anatomical regions. MC refers to the medial cortex. Note that ablation of *Kcnq2* led to a large and uniform increase of the calcium response amplitude and duration. Additional details on the statistical analysis and number of replicates for this figure are found in Table 1 under the Figure 2 section.

Figure 3. Deletion of *Kcnq2* leads to low-frequency calcium oscillations. Deletion of *Kcnq2* increased the likelihood of low-frequency oscillations across a large number of ROIs; oscillations were sustained throughout the duration of the recording period. All recordings were in the presence of 8 mM Ko. **(A)** Wavelets from control and *Pyr:Kcnq2* hemispheres. The wavelets were generated from the examples shown in Figure 2A. Note the large increase in the power for the oscillations occurring at the low-frequency range in the hemisphere from *Pyr:Kcnq2* animals. Although in this example some increases in the power were also observed at the higher-frequency values, this was not seen across all slices, as shown in panel C right panels. **(B)** Comparison of the probability density of the frequency f of transient oscillations (left panels) and the number of ROIs undergoing sustained oscillations (right panels) for the examples depicted in panel A. **(C)** Left, comparison of the probability density of the transient

eNeuro Accepted Manuscript

oscillations for control (n=43) and *Pyr:Kcnq2* hemispheres (n=47) across multiple slices. Data are represented as mean ± s.e.m. Middle and right panels show summary graphs quantifying the power measured for the two frequency domains, 0.02-0.2 Hz and 0.2-2 Hz. Note that loss of *Kcnq2* increased the likelihood of observing low-frequency calcium oscillations ranging primarily from 0.03 Hz to 0.05 Hz. **(D)** Left, comparison of the ROIs undergoing sustained oscillations for control (n=43) and *Pyr:Kcnq2* (n=47) hemispheres. Results are reported for sustained oscillations whose frequency f^* is in the LF and the HF range, respectively. See Methods section ("Time-frequency analysis") for a definition of the frequency f^* of a sustained oscillation. Middle and right panels show summary graphs of the ROIs at two frequency domains, 0.02-0.2 Hz and 0.2-2 Hz. Note that deletion of *Kcnq2* leads to a greater number of forebrain regions that show sustained low-frequency calcium oscillations (from 0.012-0.05 Hz). This is in contrast to control slices that exhibit oscillation frequencies across a wider range of frequencies (from 0.012-1.2 Hz). Additional details on the statistical analysis and number of replicates for panels C and D are found in Table 1 under the Figure 3 section.

Figure 4. **GABAA receptors limit activity in neonatal control and *Pyr:Kcnq2* brain slices.** All recordings were in the presence of 8 mM Ko. **(A)** Panels show examples of acute slices from control and *Pyr:Kcnq2* mice before and after application of 50 μM PTX to block GABAA receptors. Top panels show hemispheres segmented into ROIs. Bottom panels show 2D plots representing the changes in the calcium activity (ΔF/F) across the different ROIs upon application of PTX. The numbering corresponds to the segmented area shown on top with lower values towards the AC and higher values

eNeuro Accepted Manuscript

941 towards the PC. Note that inhibiting GABAA receptors led to widespread calcium activity
942 in the *Pyr:Kcnq2* hemisphere. In contrast, the activity in the control hemisphere was
943 primarily confined to the posterior cortex and the hippocampal formation following
944 application of PTX. **(B)** Calcium responses from the different anatomical regions before
945 and after application of PTX. Note that in *Pyr:Kcnq2* slices application of PTX led to the
946 appearance of a barrage of activity across all regions. **(C)** Scatter plots show the effect
947 of PTX on the ΔF/F amplitude and duration. Note that application of PTX increased the
948 number of larger and faster calcium signals. Additional details on the statistical analysis
949 and number of replicates for this figure are found Table 1 under the Figure 4 section.
950
951 **Figure 5. GABAA receptor activity limits the power but not the occurrence of low-**
952 **frequency calcium oscillations in *Pyr:Kcnq2* slices.** All recordings were in the
953 presence of 8 mM Ko. **(A)** Representative examples show calcium activity (ΔF/F) over
954 time and the corresponding wavelets in the presence and absence of 50 μM PTX for
955 control and *Pyr:Kcnq2* slices. Note the large increase in power at the low frequency
956 range in *Pyr:Kcnq2* slices, further quantified across multiple slices in panel C. **(B)**
957 Comparison of the probability density of the frequency f for transient oscillations before
958 and after PTX in control (n=20) and *Pyr:Kcnq2* (n=14) hemispheres. Data are
959 represented as mean ± s.e.m. The absence of change in the probability density upon
960 blocking GABAA receptor activity suggests that GABAA receptors alter the peak
961 oscillation frequency at the different ROIs. **(C)** Summary graphs show that application of
962 PTX increased the power for the low- and high-frequency domains in control and
963 *Pyr:Kcnq2* slices. **(D)** Summary graphs show that upon application of PTX the number

eNeuro Accepted Manuscript

964 of ROIs undergoing sustained oscillations in control and *Pyr:Kcnq2* slices did not
965 change. Together, (C) and (D) suggest that blocking GABAA receptors primarily
966 increases the activity within each ROI. Data are presented as mean ± s.e.m. Additional
967 details on the statistical analysis for panels C and D are found in Table 1 under the
968 Figure 5 section.
969
970 **Figure 6**. ***Kcnq2* deficient slices acquired NMDA receptor independent calcium**
971 **activities.** All recordings were in the presence of 8 mM Ko. **(A)** Panels show examples
972 of acute slices from control and *Pyr:Kcnq2* mice before and after application of 25 μM
973 D-APV (APV). Top panels show hemispheres segmented into ROIs. Bottom panels
974 show 2D plots representing the ΔF/F as a function of time for the different ROIs. The
975 numbering corresponds to the segmented area shown on top with lower values towards
976 the anterior cortex (AC) and higher values towards the posterior cortex (PC). **(B)**
977 Temporal evolution of calcium activity (ΔF/F) for the different anatomical regions before
978 and after application of APV. Note that application of APV did not prevent the
979 occurrence of large slow calcium events. **(C)** Scatter plots show the effect of APV on the
980 amplitude and duration of the calcium events across the different anatomical regions.
981 Note that blocking NMDA receptors primarily targeted calcium events with faster
982 durations (i.e., less than 10 s). In the medial cortex (MC) from control slices, application
983 of APV eliminated all activity. The ΔF/F amplitude at the PC in the presence of APV
984 went below the cut-off threshold of 0.01 ΔF/F; thus, these data points are not shown.
985 Additional details on the statistical analysis are found in Table 1 under the Figure 6
986 section.

eNeuro Accepted Manuscript

Figure 7. Blocking NMDA receptors does not prevent the emergence of slow oscillatory calcium activity in *Pyr:Kcnq2* slices. All recordings were in the presence of 8 mM Ko. **(A)** Representative examples of control and *Pyr:Kcnq2* 2D plots show calcium activity across ROIs and the corresponding wavelets. 2D plots and wavelets before and after application of 25 μM D-APV (APV) are shown. Note that APV reduced the power of the slow oscillatory activity in *Pyr:Kcnq2* slices. **(B)** Comparison of the probability density for the transient oscillation frequency (f) in the presence and absence of APV in control (n=20) and *Pyr:Kcnq2* (n=14) hemispheres. Note that APV did not change the likelihood of the emergence of a slow oscillatory activity at the 0.03 Hz to 0.05 Hz frequency range. **(C)** Summary graphs show the effect of APV in control and *Pyr:Kcnq2* hemispheres on the power at the low- (0.02-0.2 Hz) and high-frequency (0.2-2 Hz) domains. Note that APV reduced the power across all oscillatory frequencies, suggesting that NMDA receptors promote the calcium activity. **(D)** Summary graphs show the effect of APV on the number of ROIs in control and *Pyr:Kcnq2* slices, demonstrating sustained oscillations at frequency *f**. Note that blocking NMDA receptors led to a decrease in the number of ROIs undergoing sustained oscillations in *Pyr:Kcnq2* hemispheres, consistent with our observed reduction in power shown in (C). Data are represented as mean ± s.e.m. Additional details on the statistical analysis for panel C are found in Table 1 under the Figure 7 section.

Figure 8. Calcium activity is maintained in the presence of fast excitatory transmission blockers, but eliminated by TTX in slices from *Pyr:Kcnq2* mice. All

eNeuro Accepted Manuscript

recordings were in the presence of 8 mM Ko. **(A)** Top panels show representative examples of control and *Pyr:Kcnq2* slices demonstrating calcium activity across all ROIs in the presence and absence of 50 μM PTX followed by 25 μM D-APV and 25 μM NBQX. The numbering corresponds to the segmented area shown on the left with lower values towards the anterior cortex (AC) and higher values towards the posterior cortex (PC). **(B)** Calcium activity (ΔF/F) across multiple ROIs representing different forebrain anatomical areas in the presence and absence of the GABAA receptor blocker PTX (middle panels) and glutamatergic transmission blockers APV and NBQX (right panels). Note that APV/NBQX primarily inhibited the smaller and faster calcium events that had emerged in the presence of PTX in *Pyr:Kcnq2* slices. Summary information regarding the amplitude, duration, and event frequency for multiple slices is found in Table 1 under the Figure 8 section. **(C)** 1 μM TTX (n=6 slices) abolishes the calcium responses in slices pre-incubated with PTX/APV/NBQX.

Figure 9. Differential effects of fast synaptic receptor blockers on the oscillation frequencies in control and *Pyr:Kcnq2* slices. All recordings were in the presence of 8 mM Ko. **(A)** Representative examples of control and *Pyr:Kcnq2* 2D plots and their corresponding wavelets in the presence and absence of 50 μM PTX, 25 μM D-APV, and 25 μM NBQX (PTX/APV/NBQX). Note that application of all synaptic blockers reduced the power at low frequencies, but did not prevent the emergence of slow oscillatory activity in the *Pyr:Kcnq2* hemisphere. **(B)** Comparison of the probability density of the frequency f of transient oscillations before and after application of PTX/APV/NBQX in control (n=18) and *Pyr:Kcnq2* (n=14) hemispheres. **(C)** Summary graphs show the

eNeuro Accepted Manuscript

effect of PTX/APV/NBQX on the power in control and *Pyr:Kcnq2* hemispheres for the low- (0.02-0.2 Hz) and high-frequency (0.2-2 Hz) domains. **(D)** Summary graphs show the effect of PTX/APV/NBQX on the number of ROIs undergoing sustained oscillations in control and *Pyr:Kcnq2* hemispheres. Data are presented as mean ± s.e.m. Additional details on the statistical analysis for panels C and D are found in Table 1 under the Figure 9 section.

Figure 10. Ablation of *Kcnq3* leads to hyperexcitability across the forebrain in the presence of 8 mM Ko. **(A)** Top panels show two examples of acute slices from *Kcnq3*$^{+/+}$ and *Kcnq3*$^{-/-}$ mice with one hemisphere segmented into ROIs. Below, 2D plots show the changes in the ΔF/F as a function of time for the different ROIs. Note that calcium activity is recorded across all regions in the *Kcnq3*-null slice. **(B)** Raw traces show calcium activity (ΔF/F) across the different anatomical areas. Top two panels show the temporal evolution of LFPs and ΔF/F recorded in parallel from the CA3 region of the hippocampus. **(C)** Violin plots show the effect of *Kcnq3* deletion on the ΔF/F amplitude, duration, and event frequency (events/s) for the different anatomical regions. The median and the interquartile ranges are also shown. Additional details on the statistical analysis for panel C are found in Table 1 under the Figure 10 section.

Figure 11. Loss of *Kcnq3* leads to low-frequency calcium oscillations in multiple ROIs. All recordings were in the presence of 8 mM Ko. **(A)** Representative examples of *Kcnq3*$^{+/+}$ and *Kcnq3*$^{-/-}$ ΔF/F 2D plots and wavelets. Top panels show the ROIs used to generate the ΔF/F 2D plots and the wavelets. **(B)** Comparison of the probability density

eNeuro Accepted Manuscript

of the frequency f of transient oscillations and number of ROIs undergoing sustained oscillations for the examples shown in panel A. **(C)** Left, comparison of the probability density of the frequency f of transient oscillations for *Kcnq3*$^{+/+}$ (n=24) and *Kcnq3*$^{-/-}$ (n=24) across multiple hemispheres. Right, comparison of ROIs undergoing sustained oscillations for *Kcnq3*$^{+/+}$ (n=24) and *Kcnq3*$^{-/-}$ (n=24) hemispheres at different frequencies. **(D)** Left panels show summary graphs of the power at two frequency domains, 0.02-0.2 Hz and 0.2-2 Hz. Right panels show summary graphs of the ROIs exhibiting sustained oscillations at frequency f^* in the range of 0.02-0.2 Hz and 0.2-2 Hz. Additional details on the statistical analysis for panel D are found in Table 1 under the Figure 11 section.

Figure 12. Synaptic blockers inhibit calcium activity in a region-specific manner in *Kcnq3*$^{-/-}$ slices. All recordings were in the presence of 8 mM Ko. **(A)** Top two panels show the recorded LFP and $\Delta F/F$ activity from the CA3 region of the hippocampus. Middle and bottom panels show the temporal evolution of the $\Delta F/F$ across different anatomical areas. Note that synaptic blockers (PTX/APV/NBQX) abolish the calcium activity only in the medial cortex (MC) and anterior cortex (AC). **(B)** Box plots show the effect of *Kcnq3*$^{-/-}$ ablation on the $\Delta F/F$ amplitude, and event frequency for the different anatomical regions. Note that although application of synaptic blockers did not inhibit the amplitude of calcium events equally across the different regions, it did lead to a decrease to the number of calcium events across all regions. Additional details on the statistical analysis and number of replicates for panel B are found in Table 1 under the Figure 12 section.

eNeuro Accepted Manuscript

Figure 13. In *Kcnq3*$^{-/-}$ slices synaptic blockers substantially reduce slow calcium oscillations in the neocortex. All recordings were in the presence of 8 mM Ko. **(A)** Representative examples of control and *Kcnq3*$^{-/-}$ 2D plots along with their corresponding wavelets in the presence and absence of 50 μM PTX, 25 μM D-APV, and 25 μM NBQX (PTX/APV/NBQX). **(B)** Comparison of the probability density of the frequency f of transient oscillations before and after addition of PTX/APV/NBQX in *Kcnq3*$^{+/+}$ (n=18) and *Kcnq3*$^{-/-}$ (n=18) hemispheres. Note that application of the synaptic blockers did not prevent the occurrence of the slow calcium oscillations in *Kcnq3*-null slices. **(C)** Summary graphs show the effect of PTX/APV/NBQX on the power for the low- (0.02-0.2 Hz) and high-frequency (0.2-2 Hz) domains in *Kcnq3*$^{+/+}$ and *Kcnq3*$^{-/-}$ hemispheres. Note that synaptic blockers reduce the power across the board, consistent with the large reduction of the activity in the neocortex. **(D)** Summary graphs show the effect of PTX/APV/NBQX on the number of ROIs in *Kcnq3*$^{+/+}$ and *Kcnq3*$^{-/-}$ hemispheres that showed sustained oscillations at different frequencies. Data are presented as mean ± s.e.m. Additional details on the statistical analysis for panels C and D are found in Table 1 under the Figure 13 section.

Movie 1. Representative imaging showing the forebrain calcium activity in control slices in the presence of 8 mM Ko. Note the activity in the hippocampal formation. Movie played at 5x speed.

eNeuro Accepted Manuscript

Movie 2. Representative imaging showing the forebrain calcium activity in *Pyr:Kcnq2* slices in the presence of 8 mM Ko. Note the migrating activity across the neocortex. Movie played at 5x speed.

Movie 3. Representative imaging showing the forebrain calcium activity in the absence of *Kcnq2* in excitatory neurons and in the presence of synaptic blockers PTX, APV, and NBQX. Movie played at 5x speed.

Movie 4. Representative imaging showing the forebrain calcium activity in the absence of *Kcnq3*. Movie played at 5x speed.

Table 1. Summary data and statistical analysis for Figures 1-13.

Figures			Values		Statistical tests		
FIGURE 1							
			Control	***Pyr:Kcnq2***			
1B	CA3	Duration	1.6 ± 0.46 s	2.2 ± 0.35 s	Mann-Whitney U test	p=0.26	Control: n=10; *Pyr:Kcnq2*: n=18 hemispheres
		Events/s	0.0054 ± 0.0015	0.013 ± 0.0025	Mann-Whitney U test	p=0.0143	Control: n=22; *Pyr:Kcnq2*: n=21 hemispheres
	Post. Cortex	Duration	1.15 ± 0.24 s	5.3 ± 0.61 s	Mann-Whitney U test	p<0.0001	Control: n=15; *Pyr:Kcnq2*: n=20 hemispheres
		Events/s	0.008 ± 0.0018 Hz	0.015 ± 0.0018 Hz	Mann-Whitney U test	p=0.0039	Control: n=22; *Pyr:Kcnq2*: n=20 hemispheres

eNeuro Accepted Manuscript

							Animals: Control: n=6; *Pyr:Kcnq2*: n=6.
1C	CA3	APs vs current injections			Two-way ANOVA	(p=0.0025; F (9, 33) = 3.745)	Control: n=5; *Pyr:Kcnq2*: n=6 cells

FIGURE 2

			Control	***Pyr:Kcnq2***	**Statistical tests and values**		
2C	CA3	Amplit.	0.064 ± 0.007 △F/F	0.14 ± 0.014 △F/F	Mann-Whitney U test	p<0.0001	Control: n=46; *Pyr:Kcnq2*: n=56 hemispheres
		Duration	1.4 ± 0.18 s	8.5 ± 0.68 s	Mann-Whitney U test	p<0.0001	
		Events/s	0.26 ± 0.023 Hz	0.043 ± 0.0047 Hz	Mann-Whitney U test	p<0.0001	
	Post. Cortex (PC)	Amplit.	0.08 ± 0.006 △F/F	0.29 ± 0.023 △F/F	Mann-Whitney U test	p<0.0001	Control: n=44; *Pyr:Kcnq2*: n=56 hemispheres
		Duration	2.2 ± 0.19 s	6.5 ± 0.37 s	Mann-Whitney U test	p<0.0001	
		Events/s	0.14 ± 0.0072 Hz	0.048 ± 0.0032 Hz	Mann-Whitney U test	p<0.0001	
	Medial Cortex (MC)	Amplit.	0.021 ± 0.01 △F/F	0.33 ± 0.029 △F/F	Mann-Whitney U test	p<0.0001	Control, n=43; *Pyr:Kcnq2*: n=55 hemispheres
		Duration	1.4 ± 0.58 s	9.5 ± 0.56 s	Mann-Whitney U test	p<0.0001	
		Events/s	0.0065 ± 0.0024 Hz	0.018 ± 0.0023 Hz	Mann-Whitney U test		
	Anter. Cortex (AC)	Amplit.	0.02 ± 0.003 △F/F	0.36 ± 0.03 △F/F	Mann-Whitney U test	p<0.0001	Control: n=44; *Pyr:Kcnq2*: n=54 hemispheres
		Duration	1.5 ± 0.3 s	11.2 ± 0.8 s	Mann-Whitney U test	p<0.0001	
		Events/s	0.012 ± 0.0021 Hz	0.021 ± 0.0025 Hz	Mann-Whitney U test	p=0.0005	
Data were obtained from 8 control and 9 *Pyr:Kcnq2 mice*.							

FIGURE 3

		Control	***Pyr:Kcnq2***	**Statistical tests and values**		
3C	Power 0.02-0.2 Hz	0.022 ± 0.0015 A.U.	0.11 ± 0.0046 A.U.	Mann-Whitney U test	p<0.0001	Control, n=43; *Pyr:Kcnq2*:, n=47 hemispheres
	Power 0.2-2 Hz	0.026 ± 0.011 A.U.	0.38 ± 0.012A.U.	Mann-Whitney U	p<0.0001	

eNeuro Accepted Manuscript

					test		
3D	ROI 0.02-0.2 Hz		10.1 ± 0.7 ROIs	19.9 ± 0.7 ROIs	Mann-Whitney U test	p<0.0001	Control, n=43; *Pyr:Kcnq2*:, n=47 hemispheres
	ROI 0.2-2 Hz		6.6 ± 0.5 ROIs	0.5 ± 0.2 ROIs	Mann-Whitney U test	p<0.0001	
Data were obtained from 8 control and 9 *Pyr:Kcnq2 mice*.							
FIGURE 4							
			Control	***Pyr:Kcnq2***	**Statistical tests and values**		
4C	CA3	Amplit.	-PTX 0.057 △F/F ± 0.055 S.D.	-PTX 0.08 △F/F ± 0.09 S.D.	Mann-Whitney U test	Control p<0.0001	Control: -PTX: n=1547; +PTX: n=1322 events *Pyr:Kcnq2*: -PTX: n=224 events ; +PTX: n=523 events
			+PTX 0.27 △F/F ± 0.12 S.D.	+PTX 0.19 △F/F ± 0.09 S.D.	Mann-Whitney U test	*Pyr:Kcnq2* p<0.0001	
		Duration	-PTX 0.8 s ± 1.5 S.D.	-PTX 4.3 s ± 5.4 S.D.	Mann-Whitney U test	Control p<0.0001	
			+PTX 0.7 ± 1.7 S.D.	+PTX 1.8 ± 3.8 S.D.	Mann-Whitney U test	*Pyr:Kcnq2* p<0.0001	
	Post. Cortex	Amplit.	-PTX 0.08 △F/F ± 0.058 S.D.	-PTX 0.21 △F/F ± 0.26 S.D.	Mann-Whitney U test	Control p<0.0001	Control: -PTX: n=931; +PTX: n=777 events *Pyr:Kcnq2*: -PTX: n=223; +PTX: n=444 events
			+PTX 0.43 △F/F ± 0.20 S.D.	+PTX 0.38 △F/F ± 0.24 S.D.	Mann-Whitney U test	*Pyr:Kcnq2* p<0.0001	
		Duration	-PTX 1.9 s ± 2.4 S.D.	-PTX 5.1 s ± 4.5 S.D.	Mann-Whitney U test	Control p<0.0001	
			+PTX 0.58 s ± 1.0 S.D.	+PTX 1.5 ± 1.9 S.D.	Mann-Whitney U test	*Pyr:Kcnq2* p<0.0001	
	Medial Cortex	Amplit.	-PTX 0.053 △F/F ± 0.066 S.D.	-PTX 0.21 △F/F ± 0.25 S.D.	Mann-Whitney U test	Control p<0.0001	Control: -PTX: n=94; +PTX: n=270 events *Pyr:Kcnq2*: -PTX: n=62; +PTX: n=267 events
			+PTX 0.13 △F/F ± 0.22 S.D.	+PTX 0.27 △F/F ± 0.24 S.D.	Mann-Whitney U test	*Pyr:Kcnq2* p=0.0003	
		Duration	-PTX 0.9 s ± 0.74 S.D.	-PTX 7.8 s ± 6.7 S.D.	Mann-Whitney U test	Control p<0.0034	
			+PTX 1.3 s ± 2.3 S.D.	+PTX 2.1 ± 3.3 S.D.	Mann-Whitney U test	*Pyr:Kcnq2* p<0.0001	
	Anter. Cortex	Amplit.	-PTX 0.048 △F/F ± 0.038 S.D.	-PTX 0.16 △F/F ± 0.26 S.D.	Mann-Whitney U test	Control: p<0.0001	Control: -PTX: n=125; +PTX: n=310 events *Pyr:Kcnq2*: -PTX: n=150;
			+PTX 0.14 △F/F ± 0.1 S.D.	+PTX 0.37 △F/F ± 0.31 S.D.	Mann-Whitney U test	*Pyr:Kcnq2* p<0.0001	
		Duration	-PTX 1.0 s ± 1.3 S.D.	-PTX 4.8 s ± 6.1 S.D.	Mann-Whitney U test	Control p=0.11	

eNeuro Accepted Manuscript

			+PTX 0.8 s ± 0.9 S.D.	+PTX 5.3 ± 7.1 S.D.	Mann-Whitney U test	*Pyr:Kcnq2* p=0.87	+PTX: n=66 events
Data were obtained from 3 control and 3 *Pyr:Kcnq2 mice*.							

FIGURE 5

		Control	*Pyr:Kcnq2*	Statistical tests and values		
5C	Power 0.02-0.2 Hz	-PTX 0.02 ± 0.003 A.U.	-PTX 0.11 ± 0.01A.U.	Control Wilcoxon paired test	Control p<0.0001	Control: n=20; *Pyr:Kcnq2*: n=14 hemispheres
		+PTX 0.06 ± 0.007 A.U.	+PTX 0.18 ± 0.01 A.U.	*Pyr:Kcnq2* paired Student's t-test	p<0.0001 t=6.233, df=13	
	Power 0.2-2 Hz	-PTX 0.28 ± 0.02 A.U.	-PTX 0.37 ± 0.02 A.U.	Control Wilcoxon paired	Control p<0.0001	Control: n=20; *Pyr:Kcnq2*: n=14 hemispheres
		+PTX 0.58 ± 0.03 A.U.	+PTX 0.73 ± 0.0 A.U.6	*Pyr:Kcnq2* Wilcoxon paired test	*Pyr:Kcnq2* p<0.0001	
5D	ROI 0.02-0.2 Hz	-PTX 8.8 ± 0.7 ROIs	-PTX 23.0 ± 1.4 ROIs	Control paired Student's t-test	Control p=0.84 t=0.2042, df=19	Control: n=20; *Pyr:Kcnq2*: n=14 hemispheres
		+PTX 9.1 ± 1.1 ROIs	+PTX 25.2 ± 1.4 ROIs	*Pyr:Kcnq2* paired Student's t-test	*Pyr:Kcnq2* p=0.19 t=1.377, df=13	
	ROI 0.2-2 Hz	-PTX 7.6 ± 0.6 ROIs	-PTX 0 ROI	Control Wilcoxon paired test	Control p=0.72	Control: n=20; *Pyr:Kcnq2*: n=14 hemispheres
		+PTX 8.7 ± 1.6 ROIs	+PTX 0 ROI	*Pyr:Kcnq2* N/A	N/A	
Data were obtained from 4 control and 3 *Pyr:Kcnq2 mice*.						

FIGURE 6

			Control	*Pyr:Kcnq2*	Statistical tests and values		
6C	CA3	Amplit.	-D-APV 0.070 △F/F ± 0.069 S.D.	-D-APV 0.13 △F/F ± 0.14 S.D.	Mann-Whitney U test	Control: p<0.0001	Control: -D-APV n=1265; +D-APV: n=571 events *Pyr:Kcnq2*: -D-APV n=193; +D-APV: n=156 events
			+D-APV 0.036 △F/F ± 0.014 S.D.	+D-APV 0.09 △F/F ± 0.1 S.D.	Mann-Whitney U test	*Pyr:Kcnq2*: p<0.0001	
		Duration	-D-APV 0.88 s ± 2.0 S.D.	-D-APV 5.4 s ± 5.8 S.D.	Mann-Whitney U test	Control: p<0.0001	
			+D-APV 0.78 ± 1.2 S.D.	+D-APV 5.4 ± 7.1 S.D.	Mann-Whitney U test	*Pyr:Kcnq2*: p=0.0055	
	Post. Cortex	Amplit.	-D-APV 0.07 △F/F ± 0.049 S.D.	-D-APV 0.26 △F/F ± 0.36 S.D.	Mann-Whitney U test	Control: p<0.0001	Control: -D-APV n=543; +D-APV n=201 events
			+D-APV 0.02 △F/F ± 0.01	+D-APV 0.13 △F/F ±	Mann-Whitney U	*Pyr:Kcnq2*: p<0.0001	

eNeuro Accepted Manuscript

			S.D.	0.14 S.D.	test		*Pyr:Kcnq2*: -D-APV n=243; +D-APV n=170 events
		Duration	-D-APV 1.99 s ± 2.1 S.D.	-D-APV 5.1 s ± 4.2 S.D.	Mann-Whitney U test	Control: p<0.0001	
			+D-APV 2.5s ± 2.7 S.D.	+D-APV 10.8 ± 6.6 S.D.	Mann-Whitney U test	*Pyr:Kcnq2*: p<0.0001	
	Medial Cortex	Amplit.	-D-APV 0.11 △F/F ± 0.16 S.D.	-D-APV 0.18 △F/F ± 0.2 S.D.	Control: N/A	Control: N/A	Control -D-APV n=10; +D-APV n=0 events *Pyr:Kcnq2* -D-APV n=158; +D-APV, n=50events;
			+D-APV N/A	+D-APV 0.14 △F/F ± 0.16 S.D.	*Pyr:Kcnq2*: Mann-Whitney U test	*Pyr:Kcnq2*: p=0.22	
		Duration	-D-APV 7.8s ± 8.4 S.D.	-D-APV 6.3 ± 6.2 S.D.	Control: N/A	Control: N/A	
			+D-APV N/A	+D-APV 12.9 ± 8.4 S.D.	*Pyr:Kcnq2*: Mann-Whitney U test	*Pyr:Kcnq2*: p<0.0001	
	Anter. Cortex	Amplit.	-D-APV 0.017 △F/F ± 0.006 S.D.	-D-APV 0.31 △F/F ± 0.4 S.D.	Control: N/A	Control: N/A	Control -D-APV n=54; +D-APV n=0 events *Pyr:Kcnq2*: -D-APV n=71; +D-APV n=29 events
			+D-APV N/A	+D-APV 0.15 △F/F ± 0.19 S.D.	*Pyr:Kcnq2*: Mann-Whitney U test	*Pyr:Kcnq2*: p=0.0055	
		Duration	-D-APV 2.5 s ± 3.2 S.D.	-D-APV 8.9 s ± 7.1 S.D.	Control: N/A	Control: N/A	
			+D-APV N/A	+D-APV 13.3 ± 11 S.D.	*Pyr:Kcnq2*: Mann-Whitney U test	*Pyr:Kcnq2*: p=0.04	
Data were obtained from 3 control and 3 *Pyr:Kcnq2 mice*.							

FIGURE 7

		Control	***Pyr:Kcnq2***	**Statistical tests and values**		
7C	Power 0.02-0.2 Hz	-D-APV 0.019 ± 0.0015 A.U.	-D-APV 0.11 ± 0.0085 A.U.	Control: Wilcoxon paired	Control: p<0.0001	Control: n=20; *Pyr:Kcnq2*: n=14 hemispheres
		+D-APV 0.014 ± 0.0015 A.U.	+D-APV 0.069 ± 0.0057 A.U.	*Pyr:Kcnq2*: paired Student's t-test	*Pyr:Kcnq2*: p<0.0001, t=12.64, df=13	
	Power 0.2-2 Hz	-D-APV 0.24 ± 0.012 A.U.	-D-APV 0.39 ± 0.022 A.U.	Control: Wilcoxon paired	Control: p=0.0007	Control: n=20; *Pyr:Kcnq2*: n=14 hemispheres
		+D-APV 0.18 ± 0.017 A.U.	+D-APV 0.26 ± 0.0080 A.U.	*Pyr:Kcnq2*: Wilcoxon paired	*Pyr:Kcnq2*: p=0.0001	
7D	ROI 0.02-0.2 Hz	-D-APV 8.9 ± 0.65 ROIs	-D-APV 25.21 ± 1.3 ROIs	Control: paired Student's t-test	Control: p=0.20 t=1.32, df=19	Control: n=20; *Pyr:Kcnq2*: n=14 hemispheres
		+D-APV 7.5 ± 0.92 ROIs	+D-APV 20.71 ± 1.0	*Pyr:Kcnq2*: paired	*Pyr:Kcnq2*: p=0.0002	

eNeuro Accepted Manuscript

			ROIs	Student's t-test	t=5.22, df=13	
	Power 0.2-2 Hz	-D-APV 7.05 ± 0.54 ROIs	-D-APV 0 ROIs	Control: paired Student's t-test	Control: p=0.003 t=3.472, df=19	Control: n=20; *Pyr:Kcnq2*: n=14 hemispheres
		+D-APV 4.5 ± 0.54 ROIs	+D-APV 0.43 ± 0.2 ROIs	*Pyr:Kcnq2*: N/A	N/A	
Data were obtained from 3 control and 3 *Pyr:Kcnq2 mice.*						

FIGURE 8

P/N/A refers to Picrotoxin/APV/NBQX			**Control**	***Pyr:Kcnq2***	**Statistical tests and values**		
8B	CA3	Amplit.	-P/N/A: 0.046 Δ F/F ± 0.14 S.D.	-P/N/A:0.105 ΔF/F ± 0.14 S.D.	Mann-Whitney U test	Control: N/A	Control - P/N/A: n=444; +P/N/A: n=0 events *Pyr:Kcnq2*: - P/N/A: n=246; +P/N/A: n=38 events
			N/A	+P/N/A: ΔF/F 0.14 ± 0.13 S.D.		*Pyr:Kcnq2* p=0.0001	
		Duration	-P/N/A: 0.59 s ± 1.3 S.D.	-P/N/A: 4.5 s ± 6.7 S.D.	Mann-Whitney U test	Control: N/A	
			N/A	+P/N/A: 13.5 s ± 7.5 S.D.		*Pyr:Kcnq2*: p<0.0001	
	Post. Cortex	Amplit.	0.059 Δ F/F ± 0.03 S.D.	-P/N/A:0.48 Δ F/F ± 0.63 S.D.	Mann-Whitney U test	Control: N/A	Control - P/N/A: n=228; +P/N/A: n=0 events *Pyr:Kcnq2*: - P/N/A: n=194; +P/N/A: n=36 events
			N/A	+P/N/A: Δ 0.71 F/F ± 0.47 S.D.		*Pyr:Kcnq2*: p=0.009	
		Duration	-P/N/A: 1.66 s ± 1.7 S.D.	-P/N/A: 4.6 s ± 3.9 S.D.	Mann-Whitney U test	Control: N/A	
			N/A	+P/N/A: 10.2 s ± 3.6 S.D.		*Pyr:Kcnq2*: p<0.0001	
	Medial Cortex	Amplit.	0.028 Δ F/F ± 0.018 S.D.	-P/N/A:0.38 Δ F/F ± 0.31 S.D.	Mann-Whitney U test	Control: N/A	Control - P/N/A: n=22; +P/N/A: n=0 events *Pyr:Kcnq2*: - P/N/A: n=64; +P/N/A: n=56 events
			N/A	+P/N/A: Δ 0.19 F/F ± 0.17 S.D.		*Pyr:Kcnq2*: p=0.005	
		Duration	-P/N/A: 0.65 s ± 0.17 S.D.	-P/N/A: 7.6 s ± 4.7 S.D.	Mann-Whitney U test	Control: N/A	
			N/A	+P/N/A: 8.9 s ± 7.5 S.D.		*Pyr:Kcnq2*: p=0.087	
	Anter. Cortex	Amplit.	0.029 Δ F/F ± 0.026 S.D.	-P/N/A:0.47 Δ F/F ± 0.48 S.D.	Mann-Whitney U test	Control: N/A	Control - P/N/A: n=22; +P/N/A: n=0 events *Pyr:Kcnq2*: - P/N/A: n=82; +P/N/A: n=43 events
			N/A	+P/N/A: Δ 0.35 F/F ± 0.38 S.D.		*Pyr:Kcnq2*: p=0.087	
		Duration	-P/N/A: 0.77 s ± 0.63 S.D.	-P/N/A: 7.7 s ± 5.8 S.D.	Mann-Whitney U test	Control: N/A	
			N/A	+P/N/A: 14.1 s ± 8.7 S.D.		*Pyr:Kcnq2*: p=0.016	

eNeuro Accepted Manuscript

Data were obtained from 3 control and 3 *Pyr:Kcnq2 mice*.							
FIGURE 9							
P/N/A refers to Picrotoxin/APV/NBQX			**Control**	***Pyr:Kcnq2***	**Statistical tests and values**		
9C	Power 0.02-0.2 Hz		-P/A/N 0.018 ± 0.0007 A.U.	-P/A/N 0.13 ± 0.0094 A.U.	Control: Wilcoxon paired	Control: p<0.0001	Control: n=18; *Pyr:Kcnq2*: n=14 hemispheres
			+P/A/N 0.01 ± 0.0006 A.U.	+P/A/N 0.068 ± 0.0083 A.U.	*Pyr:Kcnq2*: Wilcoxon paired	*Pyr:Kcnq2*: p=0.0001	
	Power 0.2-2 Hz		-P/A/N 0.22 ± 0.007 A.U.	-P/A/N 0.45 ± 0.03 A.U.	Control: paired Student's t-test	Control: p<0.0001 t=9.106, df=17	Control: n=18; *Pyr:Kcnq2*: n=14 hemispheres
			+P/A/N 0.13 ± 0.002 A.U.	+P/A/N 0.26 ± 0.01 A.U.	*Pyr:Kcnq2*: paired Student's t-test	*Pyr:Kcnq2*: p<0.0001 t=9.055, df=13	
	ROI 0.02-0.2 Hz		-P/A/N 10.17 ± 0.93 ROIs	-P/A/N 19.86 ± 1.2 ROIs	Control: Wilcoxon paired	Control: p=0.0001	Control: n=18; *Pyr:Kcnq2*: n=14 hemispheres
			+P/A/N 3.5 ± 0.85 ROIs	+P/A/N 15.14 ± 1.3 ROIs	*Pyr:Kcnq2*: paired Student's t-test	*Pyr:Kcnq2*: p=0.0092 t=3.057, df=13	
	ROI 0.2-2 Hz		-P/A/N 8.7 ± 0.7 ROIs	-P/A/N 0 ROI	Control: Wilcoxon paired	Control: p<0.0001	Control: n=18; *Pyr:Kcnq2*: n=14 hemispheres
			+P/A/N 0.72 ± 0.18 ROIs	+P/A/N 0 ROI	*Pyr:Kcnq2*: N/A		
Data were obtained from 3 control and 3 *Pyr:Kcnq2 mice*.							
FIGURE 10							
			***Kcnq3*$^{+/+}$**	***Kcnq3*$^{-/-}$**	**Statistical tests**		
10C	CA3	Amplit.	0.08 ± 0.005△F/F	0.08 ± 0.007△F/F	Welch's t-test	p=0.95, t=0.07052, df=42	*Kcnq3*$^{+/+}$, n=23; *Kcnq3*$^{-/-}$: n=21 hemispheres
		Duration	2.4 ± 0.8 s	1.2 ± 0.2 s	Mann-Whitney U test	p=0.93	
		Events/s	0.22 ± 0.03 Hz	0.19 ± 0.3 Hz	Mann-Whitney U test	p=0.05	*Kcnq3*$^{+/+}$, n=24; *Kcnq3*$^{-/-}$: n=24 hemispheres
	Post. Cortex	Amplit.	0.073 ± 0.006△F/F	0.12 ± 0.01△F/F	Mann-Whitney U test	p<0.0001	*Kcnq3*$^{+/+}$, n=23; *Kcnq3*$^{-/-}$, n=24 hemispheres
		Duration	1.4 ± 0.3 s	4.5 ± 0.9 s	Mann-Whitney U test	p<0.0001	
		Events/s	0.21 ± 0.025 Hz	0.12 ± 0.023 Hz	Mann-Whitney U	p=0.013	*Kcnq3*$^{+/+}$, n=24;

eNeuro Accepted Manuscript

					test		*Kcnq3*$^{-/-}$: n=24 hemispheres
	Medial Cortex	Amplit.	0.028 ± 0.008△F/F	0.09 ± 0.02△F/F	Mann-Whitney U test	p=0.08	*Kcnq3*$^{+/+}$, n=13; *Kcnq3*$^{-/-}$: n=21 hemispheres
		Duration	3.2 ± 1.1 s	4.3 ± 1.2 s	Mann-Whitney U test	p=0.004	
		Events/s	0.02 ± 0.12 Hz	0.017 ± 0.003 Hz	Mann-Whitney U test	p=0.009	*Kcnq3*$^{+/+}$, n=24; *Kcnq3*$^{-/-}$: n=24 hemispheres
	Anter. Cortex	Amplit.	0.03 ± 0.003△F/F	0.10 ± 0.13△F/F	Mann-Whitney U test	p<0.0001	*Kcnq3*$^{+/+}$, n=20; *Kcnq3*$^{-/-}$: n=22 hemispheres
		Duration	3.1 ± 1.0 s	5.2 ± 1.3 s	Mann-Whitney U test	p=0.72	
		Events/s	0.032 ± 0.007 Hz	0.05 ± 0.007 Hz	Mann-Whitney U test	p=0.06	*Kcnq3*$^{+/+}$, n=24; *Kcnq3*$^{-/-}$: n=24 hemispheres
Data were obtained from 4 *Kcnq3*$^{+/+}$ and 4 *Kcnq3*$^{-/-}$ *mice*.							

FIGURE 11

		***Kcnq3*$^{+/+}$**	***Kcnq3*$^{-/-}$**	**Statistical tests**		
11D	Power 0.02-0.2 Hz	0.035 ± 0.005 A.U.	0.06 ± 0.005 A.U.	Mann-Whitney U test	p<0.0001	*Kcnq3*$^{+/+}$, n=24; *Kcnq3*$^{-/-}$: n=24 hemispheres
	Power 0.2-2 Hz	0.57 ± 0.1 A.U.	0.53 ± 0.08 A.U.	Mann-Whitney U test	p=0.67	
	ROI 0.02-0.2 Hz	12 ± 1 ROIs	25 ± 1 ROIs	Mann-Whitney U test	p<0.0001	*Kcnq3*$^{+/+}$, n=24; *Kcnq3*$^{-/-}$: n=24 hemispheres
	ROI 0.2-2 Hz	6.2 ± 0.8 ROIs	0.6 ± 0.2 ROIs	Mann-Whitney U test	p<0.0001	
Data were obtained from 4 *Kcnq3*$^{+/+}$ and 4 *Kcnq3*$^{-/-}$ *mice*.						

FIGURE 12

P/N/A refers to Picrotoxin/APV/NBQX			***Kcnq3*$^{-/-}$** -blockers	***Kcnq3*$^{-/-}$** +blockers	**Statistical tests**		
12B	CA3	Amplit.	0.09 ± 0.009 △F/F	0.064 ± 0.008 △F/F	Student's t-test	p=0.054, t=2.007, df=29	*Kcnq3*$^{-/-}$: n=16; +P/A/N: n=15 hemispheres
		Duration (not illustrated)	1.1 ± 0.2 s	7.7 ± 1.6 s	Wilcoxon paired	p=0.0006	*Kcnq3*$^{-/-}$: n=16; P/A/N: n=15 hemispheres

eNeuro Accepted Manuscript

		Events/s	0.22 ± 0.03 Hz	0.019±0.3 Hz	Wilcoxon paired test	p=0.0002	*Kcnq3*$^{-/-}$ n=18; P/A/N: n=18 hemispheres
	Post. Cortex	Amplitude	0.13±0.01 △F/F	0.17±0.02 △F/F	Wilcoxon paired	p=0.15	*Kcnq3*$^{-/-}$ n=18; P/A/N: n=15 hemispheres
		Duration (not illustrated)	3.1 ± 0.8 s	9.0 ± 0.9 s	Wilcoxon paired	p=0.0006	*Kcnq3*$^{-/-}$ n=18; P/A/N: n=15 hemispheres
		Events/s	0.16±0.03 Hz	0.01±0.003 Hz	Wilcoxon paired	p<0.0001	*Kcnq3*$^{-/-}$ n=18; P/A/N: n=18 hemispheres
	Medial Cortex	Amplitude	0.12±0.02△F/F	ND	N/D	N/D	*Kcnq3*$^{-/-}$ n=18; +P/A/N: n=0 hemispheres
		Duration (not illustrated)	5.2 ± 1.6 s	ND	N/D	N/D	*Kcnq3*$^{-/-}$ n=18; P/A/N: n=0 hemispheres
		Events/s	0.02±0.004 Hz	ND	N/D	N/D	*Kcnq3*$^{-/-}$ n=18; P/A/N: n=18 hemispheres
	Anter. Cortex	Amplitude	0.1±0.1△F/F	0.07±0.02△F/F	Wilcoxon paired	p=0.88	*Kcnq3*$^{-/-}$ n=18; P/A/N: n=4 hemispheres
		Duration (not illustrated)	4.0 ± 0.7 s	9.6 ± 3.4 s	Wilcoxon paired	p=0.25	*Kcnq3*$^{-/-}$ n=18; P/A/N: n=4 hemispheres
		Events/s	0.06±0.007 Hz	0.001±0.0006 Hz	Wilcoxon paired	p<0.0001	*Kcnq3*$^{-/-}$ n=18; P/A/N: n=18 hemispheres

Data were obtained from 3 *Kcnq3*$^{+/+}$ and 3 *Kcnq3*$^{-/-}$ *mice.*

FIGURE 13

P/N/A refers to Picrotoxin/APV/NBQX		***Kcnq3*$^{+/+}$**	***Kcnq3*$^{-/-}$**	**Statistical tests**		
13C	Power 0.02-0.2 Hz	-P/A/N 0.025 ± 0.0019	-P/A/N 0.05 ± 0.003	*Kcnq3*$^{+/+}$ Wilcoxon paired	p<0.0001	*Kcnq3*$^{+/+}$ n=17; *Kcnq3*$^{-/-}$ n=16 hemispheres
		+P/A/N 0.01 ± 0.0009	+P/A/N 0.02± 0.0018	*Kcnq3*$^{-/-}$ paired Student's t-test	p<0.0001 t=9.531, df=15	
	Power 0.2-2 Hz	-P/A/N 0.33 ± 0.012	-P/A/N 0.33 ± 0.019	*Kcnq3*$^{+/+}$ paired Student's t-test	p<0.0001 t=11.60, df=16	

eNeuro Accepted Manuscript

		+P/A/N 0.19 ± 0.006	+P/A/N 0.19 ± 0.011	*Kcnq3*$^{-/-}$ paired Student's t-test	p<0.0001 t=8.787, df=15	
13D	ROI 0.02-0.2 Hz	-P/A/N 12.5 ± 0.96	-P/A/N 25 ± 1.3	*Kcnq3*$^{+/+}$ Wilcoxon paired	p=0.0004 t=4.477, df=16	*Kcnq3*$^{+/+}$ n=17; *Kcnq3*$^{-/-}$ n=16 hemispheres
		+P/A/N 6.0 ± 1.1	+P/A/N 17.7 ± 1.6	*Kcnq3*$^{-/-}$ paired Student's t-test	p=0.0006 t=4.321, df=15	
	ROI 0.2-2 Hz	-P/A/N 7.1 ± 0.92	-P/A/N 0.75 ± 0.25	*Kcnq3*$^{+/+}$ Wilcoxon paired	p<0.0001	
		+P/A/N 0.76 ± 0.22	+P/A/N 0.81 ± 0.26	*Kcnq3*$^{-/-}$ Wilcoxon paired	p=0.83	
Data were obtained from 3 *Kcnq3*$^{+/+}$ and 3 *Kcnq3*$^{-/-}$ *mice*.						

1114

eNeuro Accepted Manuscript

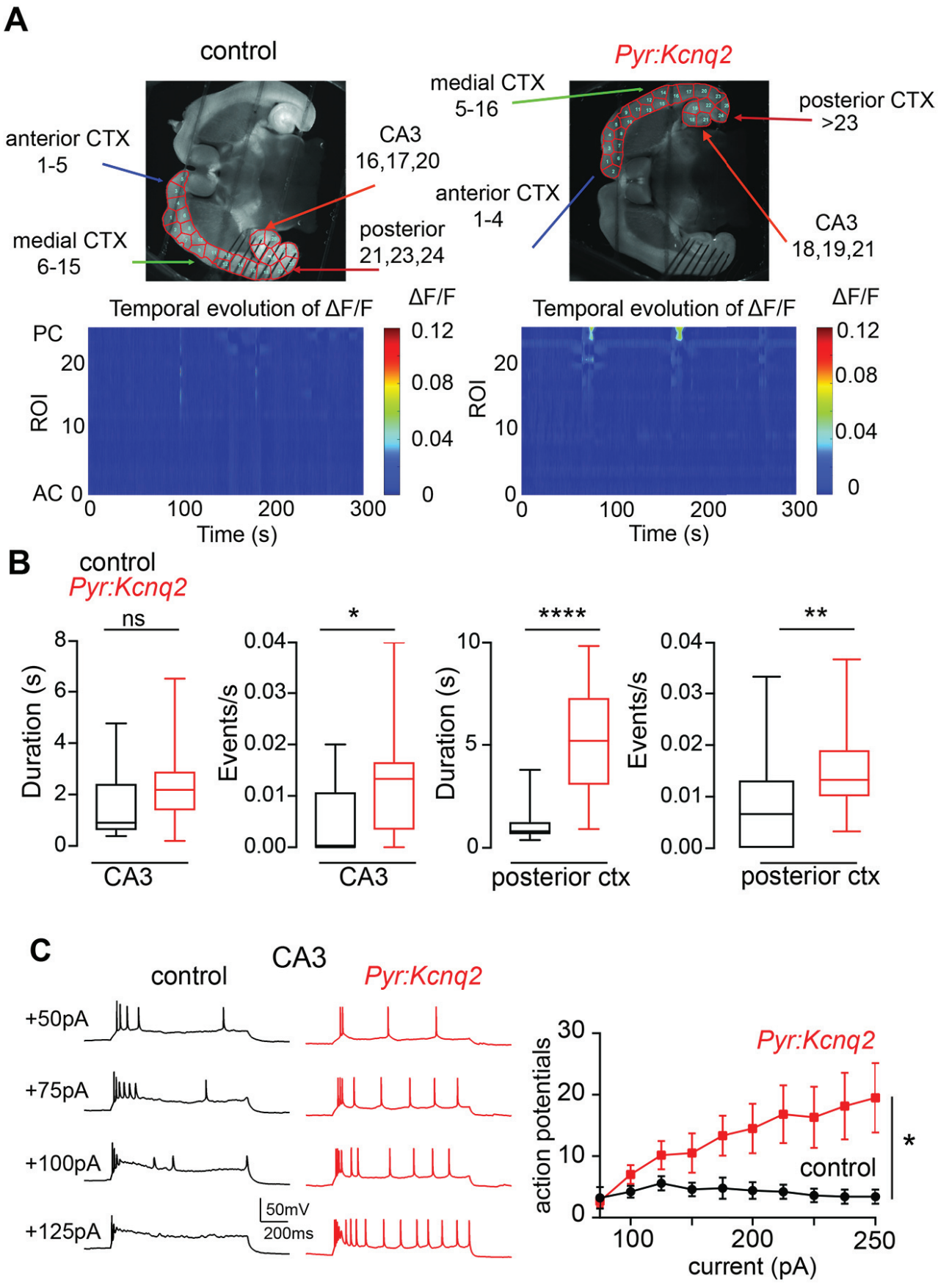

eNeuro Accepted Manuscript

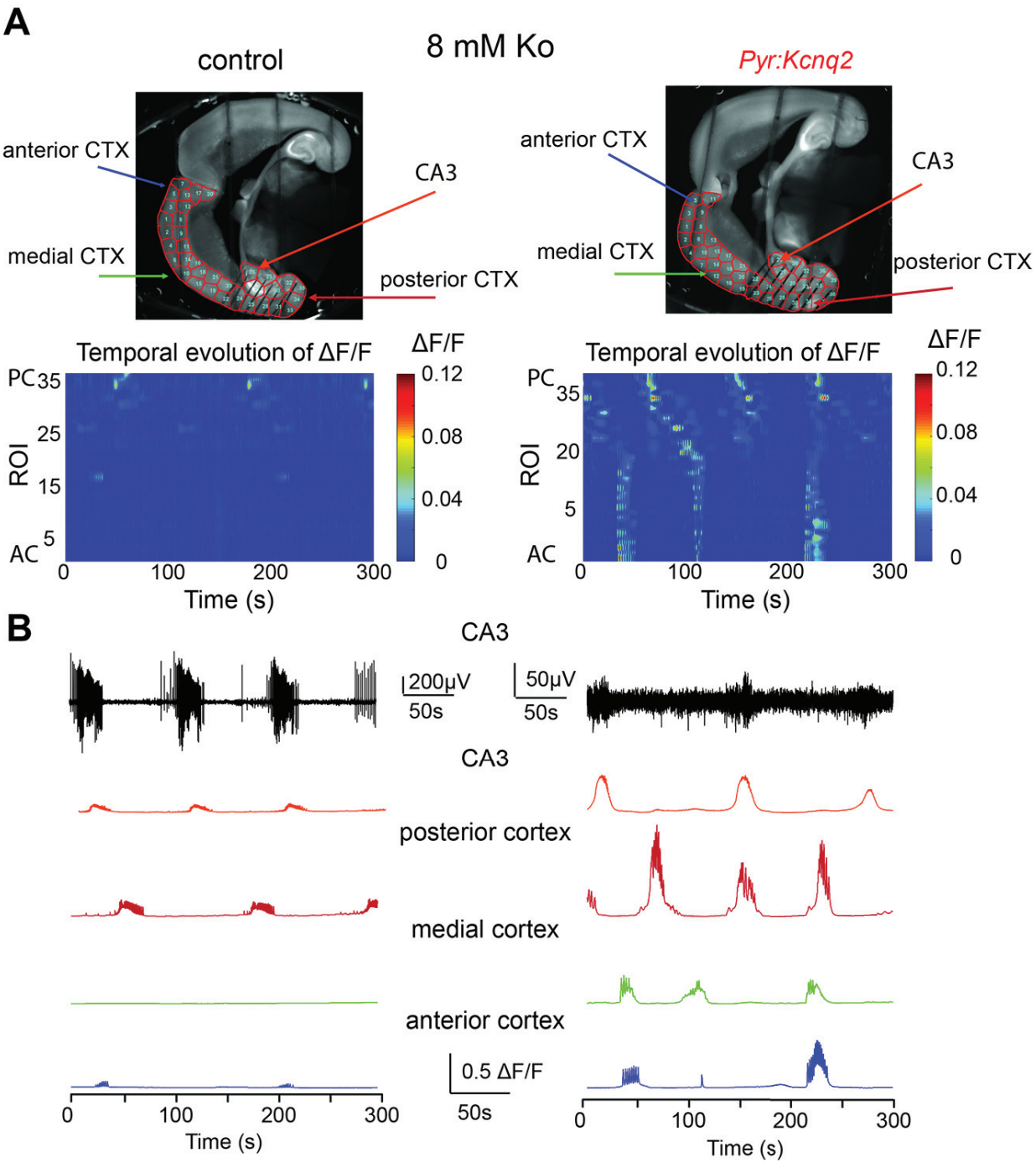

eNeuro Accepted Manuscript

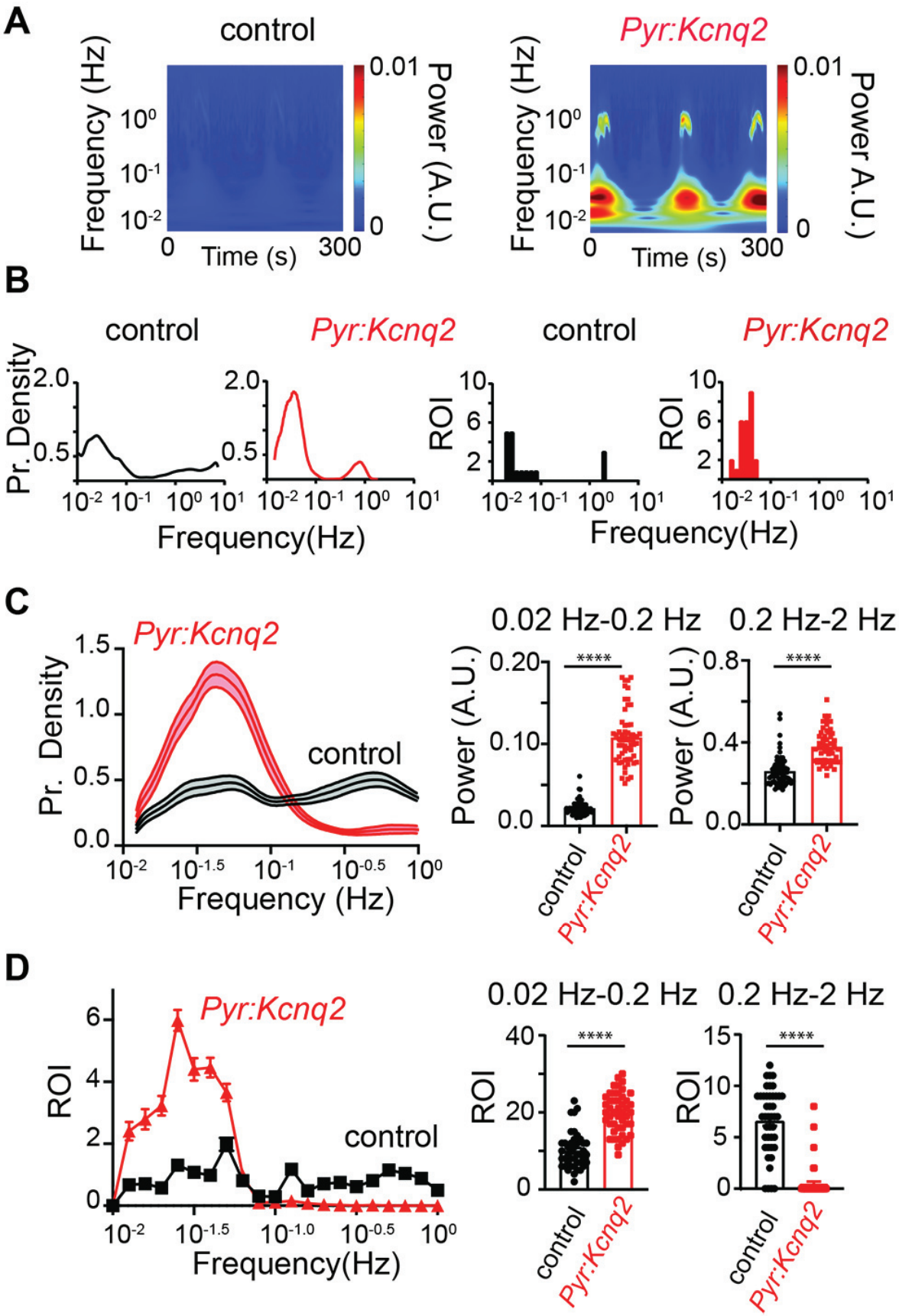

eNeuro Accepted Manuscript

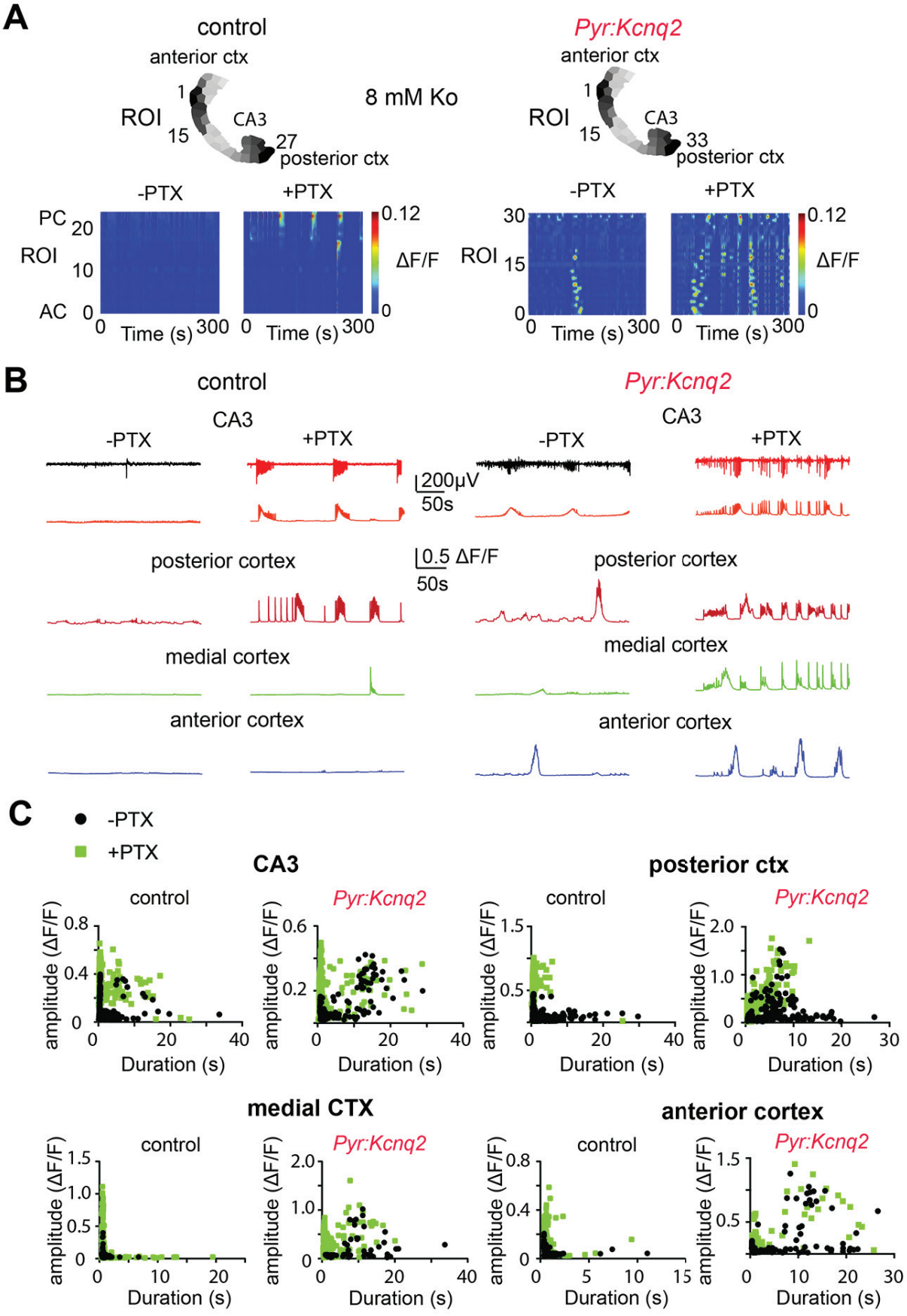

eNeuro Accepted Manuscript

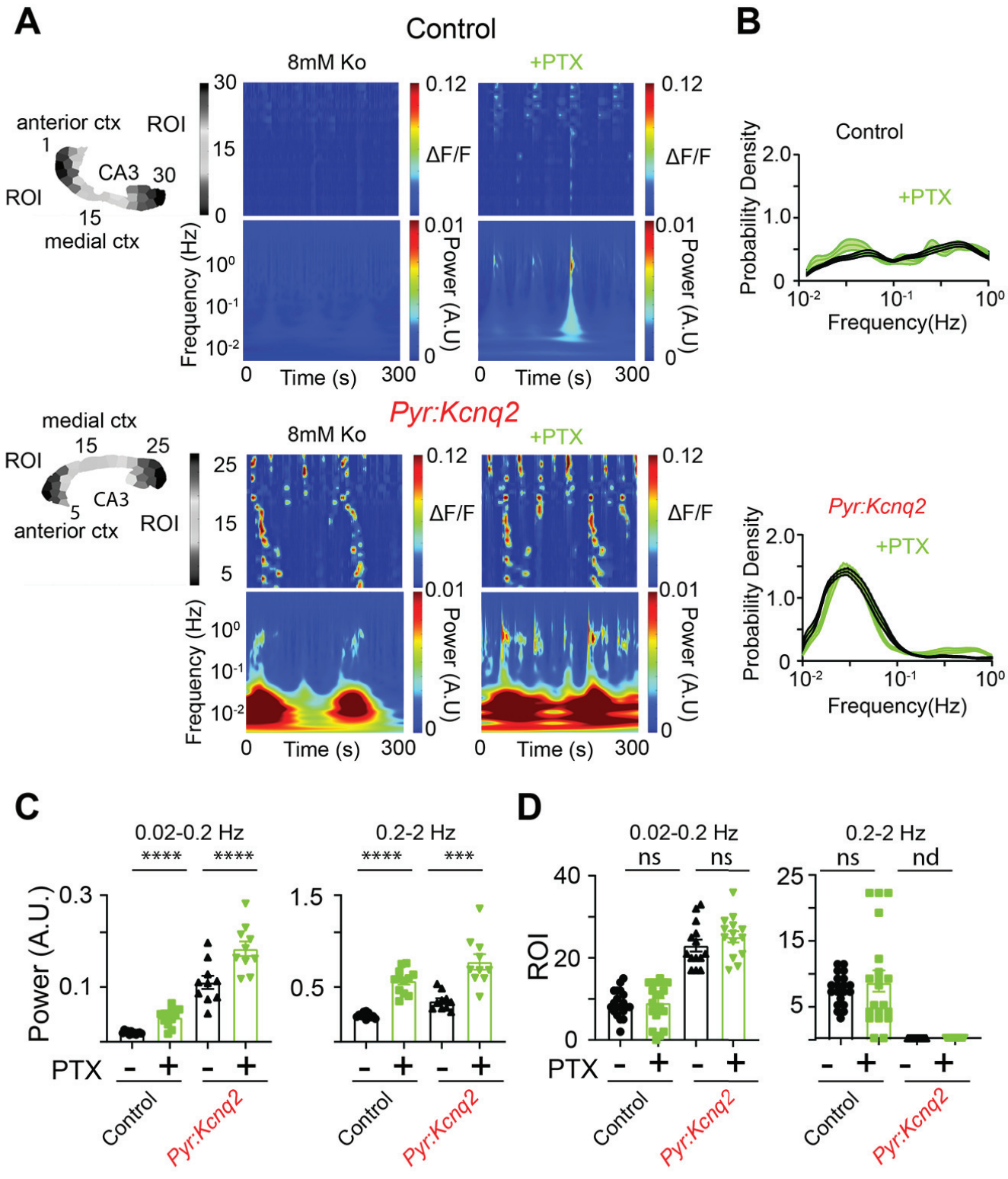

eNeuro Accepted Manuscript

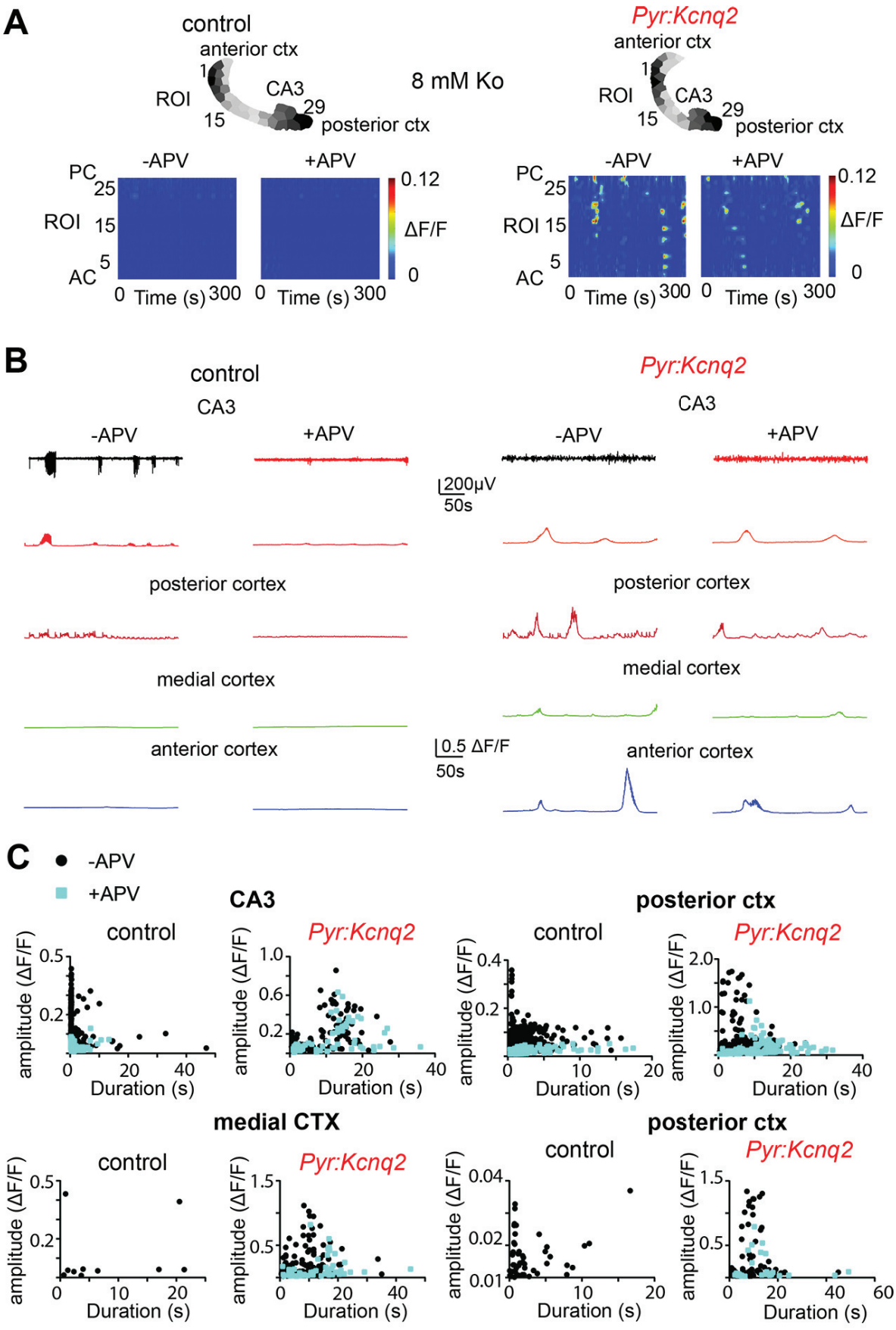

eNeuro Accepted Manuscript

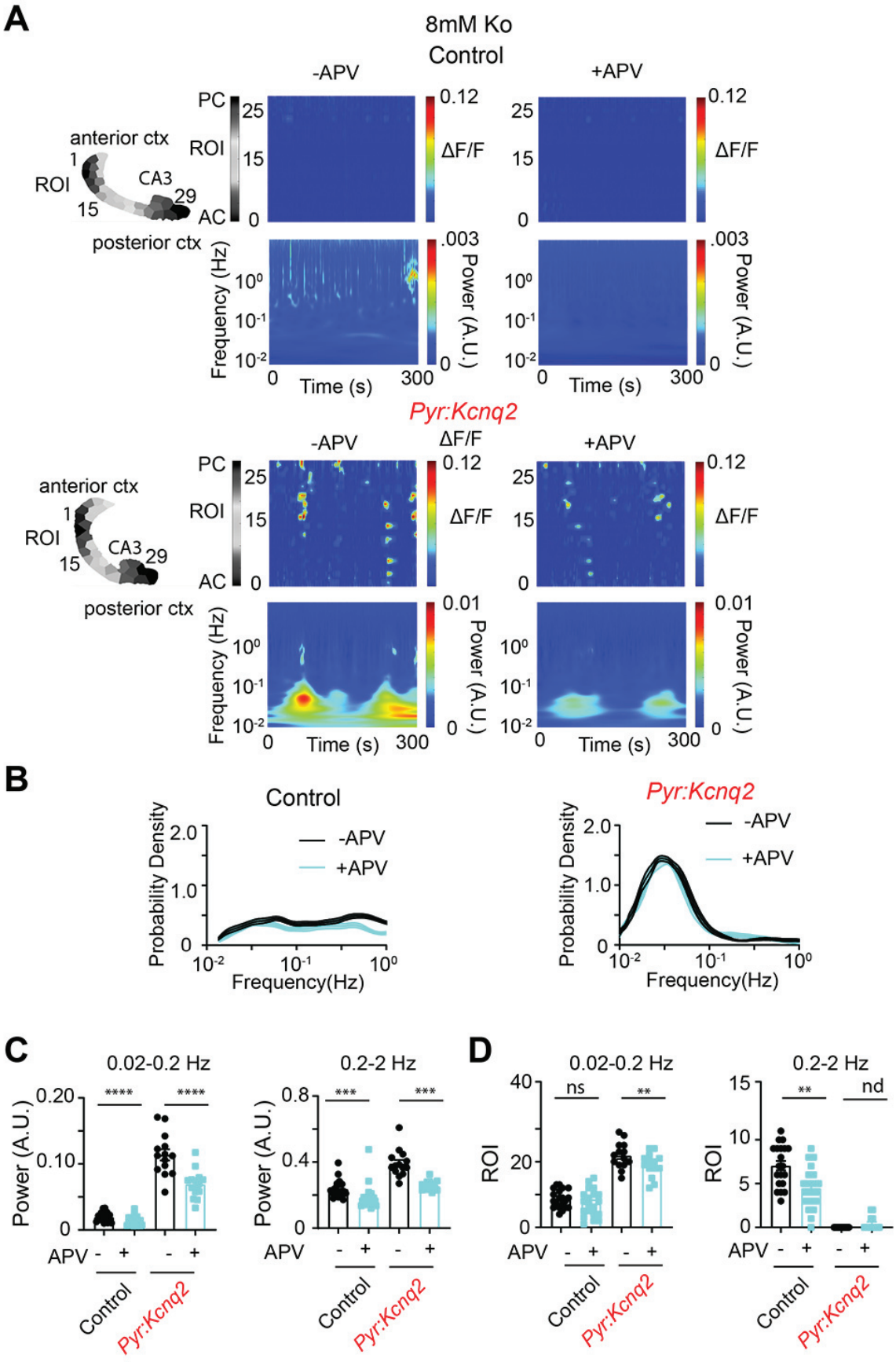

eNeuro Accepted Manuscript

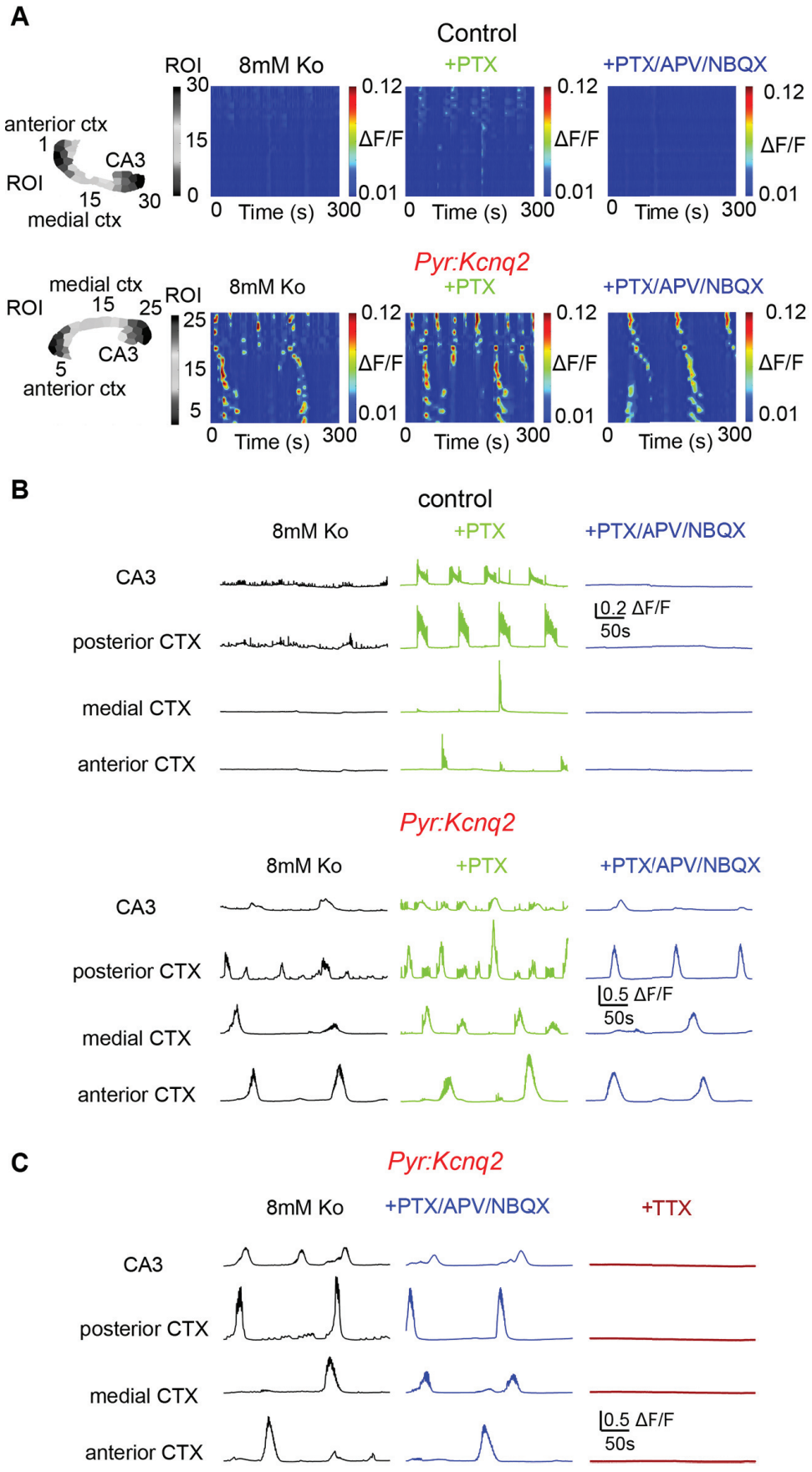

eNeuro Accepted Manuscript

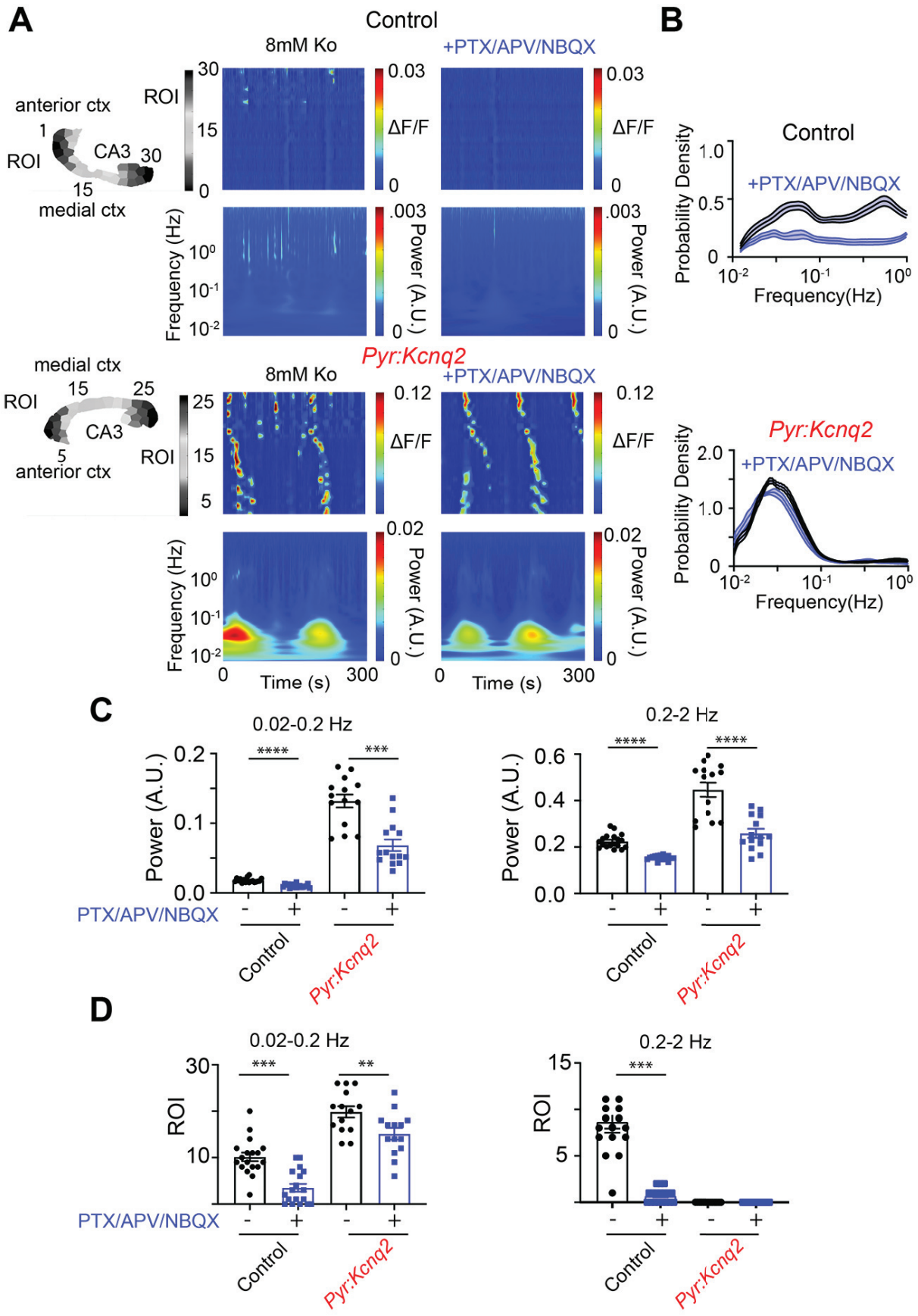

eNeuro Accepted Manuscript

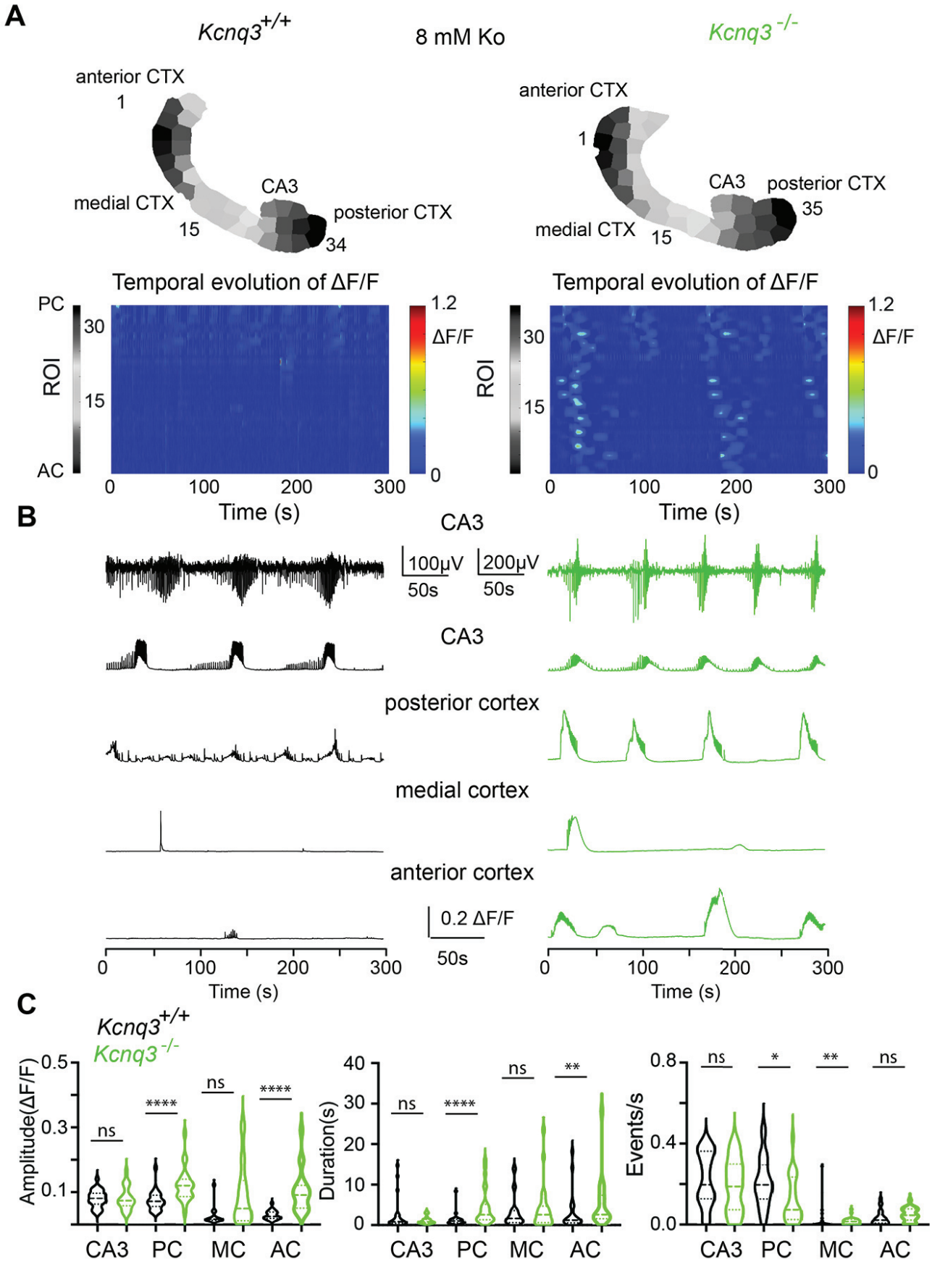

eNeuro Accepted Manuscript

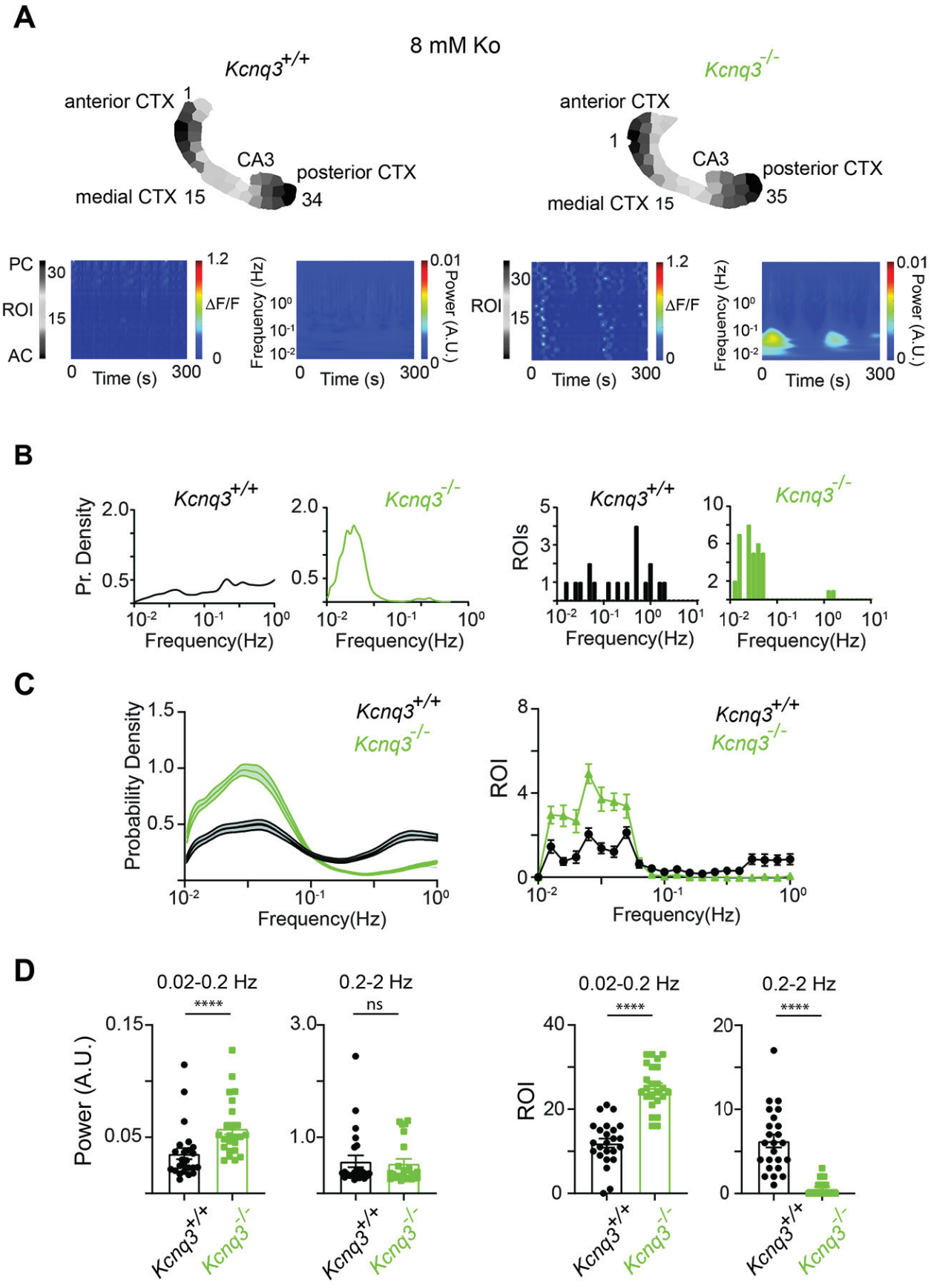

eNeuro Accepted Manuscript

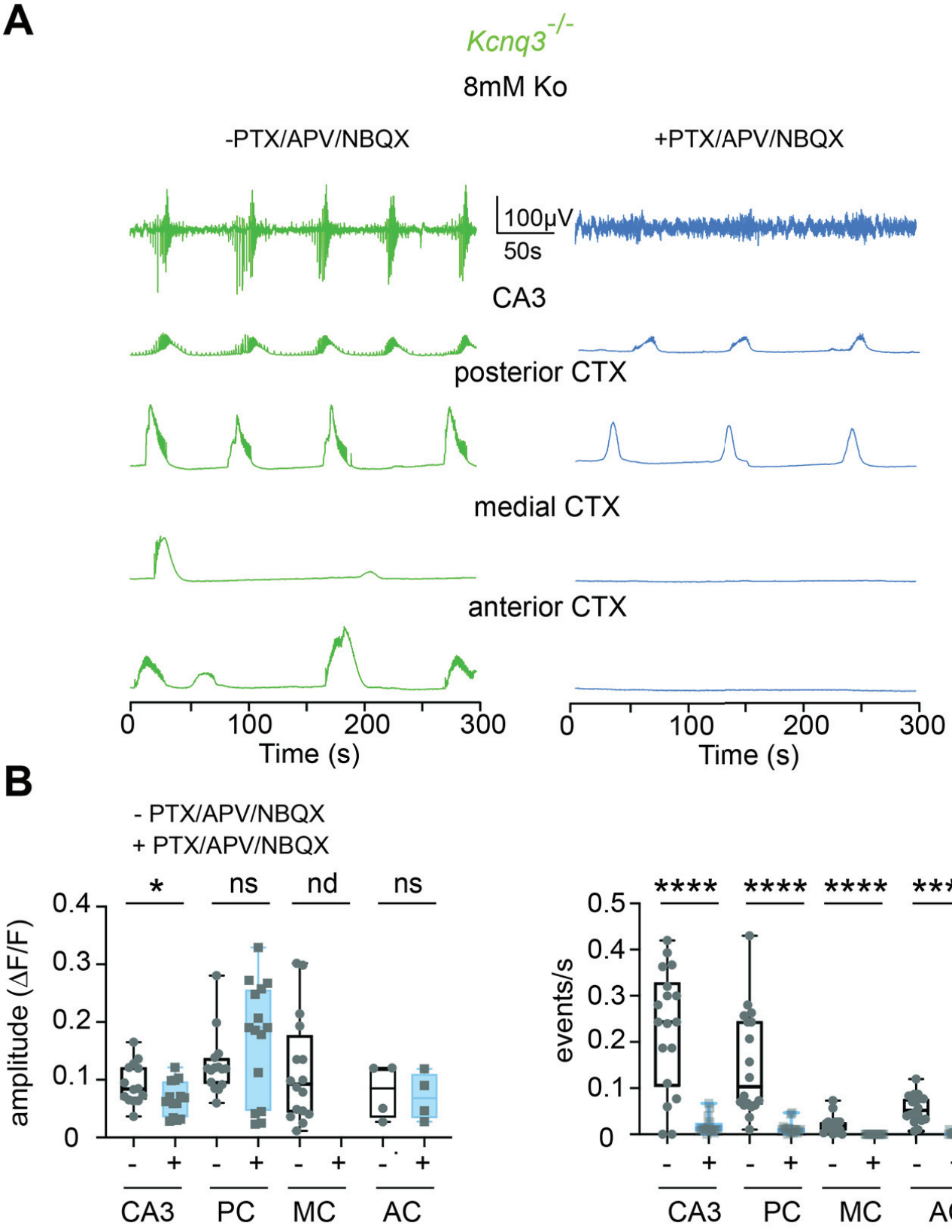
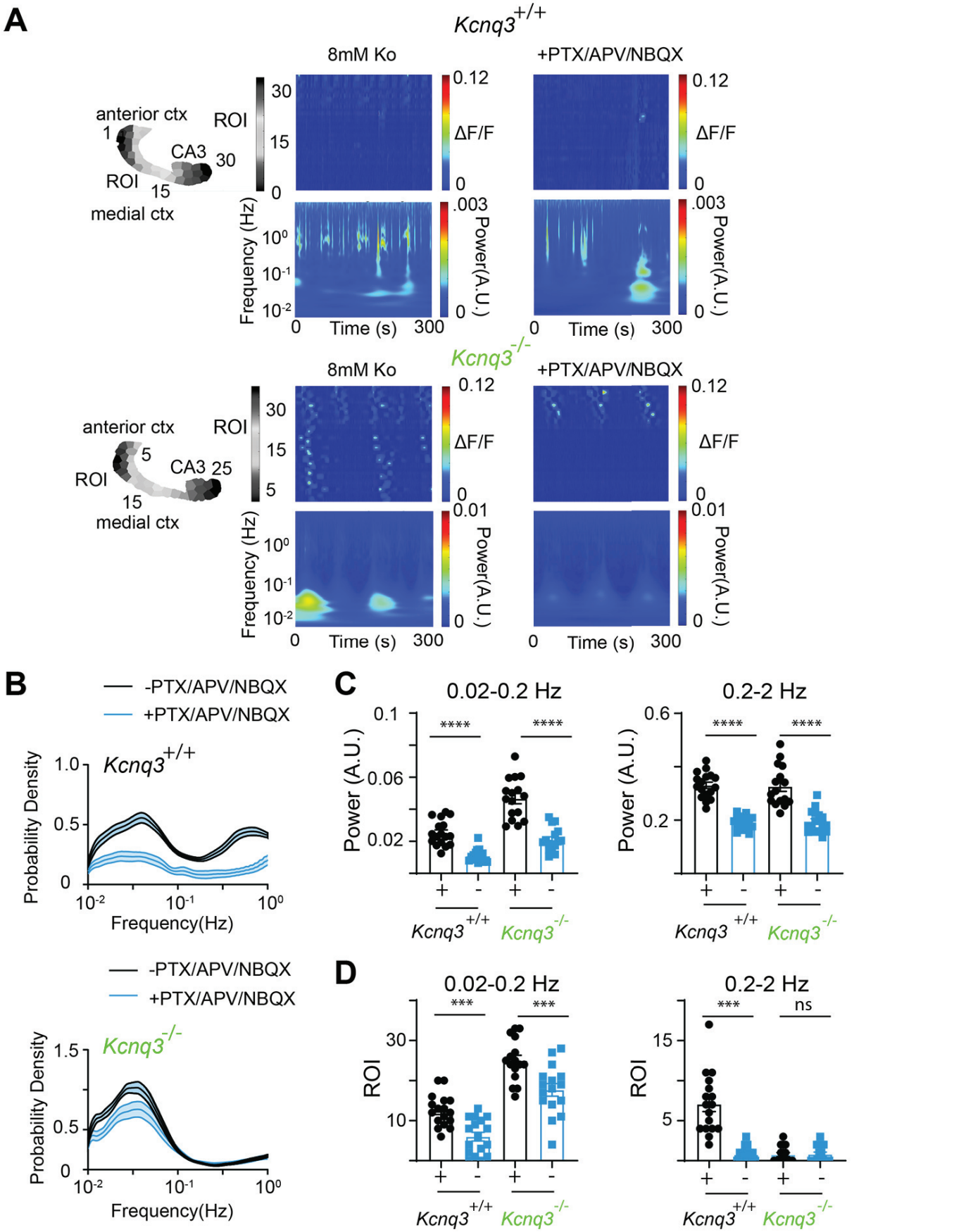
eNeuro Accepted Manuscript